Scientific Reports

https://doi.org/10.1038/s41598-026-43031-8

Article in Press

Finite element analysis of stress distributions in knee ligaments and menisci during the Taekwondo Roundhouse Kick

Received: 5 October 2025

Accepted: 28 February 2026

Published online: 13 March 2026

Cite this article as: Jia M., Li D., Ma Y. *et al.* Finite element analysis of stress distributions in knee ligaments and menisci during the Taekwondo Roundhouse Kick. *Sci Rep* (2026). https://doi.org/10.1038/s41598-026-43031-8

Mengyao Jia, Duo Li, Yong Ma, Lin Liu, Shijie Lin, Ruifeng Huang, Zhaoyi Wang, Weitao Zheng & Xin Ji

Finite Element Analysis of Stress Distributions in Knee Ligaments and Menisci During the Taekwondo Roundhouse Kick

JIA Mengyao[1,2,3], LI Duo[1,2,3*], MA Yong[1,2,3*], LIU Lin[1,2,3], LIN Shijie[4], HUANG Ruifeng[1,2,3], WANG Zhaoyi[1,2,3], ZHENG Weitao[1,2,3], JI Xin[1,2,3]

1 School of Intelligent Sports Engineering, Wuhan Sports University, Wuhan, 430079, China.

2 Hubei Engineering Research Center for Intelligent Equipment in Sports and Health, Wuhan Sports University, Wuhan, 430079, China.

3. Dongguan University of Technology, Dongguan, Guangdong, 523808.

4. Northwest Polytechnical University, Xi'an, Shanxi, 710072.

5. The Hong Kong Polytechnic University, Hong Kong, 999077.

Correspondence: 2015025@whsu.edu.cn (LD), mayong@whsu.edu.cn (MY).

Abstract: Objective To describe relative mechanical loading exposure and stress-distribution patterns in major knee ligaments and menisci during the Taekwondo Roundhouse kick at four biomechanically defined key moments (E1–E4). **Methods** Twelve elite male Taekwondo athletes performed standardized Roundhouse kicks with synchronized motion capture and ground reaction force measurement. Cohort-mean kinematics and net knee joint reaction forces estimated in OpenSim were applied to a subject-specific knee finite element (FE) model. Four independent quasi-static FE snapshots were solved at E1–E4. Model contact behavior under a 1000 N axial compression benchmark was compared with published ranges for plausibility. **Results** Across E1–E4, the supporting leg showed consistently higher stress exposure in cruciate/collateral ligaments and menisci than the attacking leg. Stress hotspots were primarily localized near ligament attachment regions and at the posterior horn/peripheral zones of the menisci, with the supporting-leg lateral meniscus demonstrating the most pronounced meniscal stress concentration. **Conclusion** The supporting knee bears the dominant mechanical demand during the Roundhouse kick, suggesting that training and technique optimization should prioritize load management of the supporting leg and control of stress exposure in key knee tissues.
Keywords: Finite element; Simulation; Biomechanics; Stress distribution; Knee joint

Background

Competitive Taekwondo is an intense combat sport and one of the most popular martial arts worldwide. It combines the spirit of Taekwondo with the high standards of the Olympic spirit [1]. The sport is characterized by dynamic full-contact sparring, where athletes employ high-frequency kicking and striking techniques, making flexibility and endurance crucial for performance [2],[3]. The objective of the match is to score the most points or win in a knockout, with the target areas being the opponent's torso and head [4].

The Roundhouse kick is one of the most frequently used techniques in competition [5], known for its simplicity, directness, strong concealment, explosive power, rapid transition between offense and defense, high scoring efficiency, and minimal vulnerability. It serves both as a primary offensive tool and as a countermeasure to disrupt an opponent's attack [6]-[8]. Although the movement appears straightforward, its execution involves coordinated hip rotation, trunk stabilization, and rapid extension of the supporting leg, which together generate considerable load on the knee joint, particularly on ligament and meniscus structures. Given its high utilization rate during matches, the Roundhouse kick often results in repeated mechanical loading, which may elevate the risk of both acute and overuse injuries.

In biomechanics, valgus stress refers to the lateral-directed force that tends to bend the knee inward, placing tension on the medial structures such as the medial collateral ligament (MCL). Internal rotation moments describe rotational forces that cause the tibia to rotate inward relative to the femur,

which can strain cruciate ligaments such as the anterior cruciate ligament (ACL). Both valgus stress and internal rotation moments are important contributors to knee ligament injury mechanisms in high-impact sports like Taekwondo.

Since the International Olympic Committee (IOC) initiated the injury surveillance system, Taekwondo has consistently ranked among the Olympic sports with the highest injury rates [9]. Injuries directly impact the performance of elite athletes, a challenge shared by many sports [10]. Injuries significantly affect athletes' performance, and in Taekwondo, the knee joint is frequently reported as one of the most vulnerable anatomical sites. Ligament injuries are commonly observed [11]. Studies have also indicated a strong association between ligament injuries and concurrent meniscal damage[12],[13]. For instance, anterior cruciate ligament (ACL) injuries are accompanied by meniscal lesions in approximately 39.5% of cases [14]. while medial meniscus root tears are reported in 2.74% of patients with ligament injuries [15], highlighting a biomechanical interdependence between these structures.

In response to the high incidence of injuries, the World Taekwondo Federation (WTF) has revised competition rules multiple times, prompting athletes to adjust their training approaches and tactical decisions. These rule changes have influenced the types and mechanisms of knee injuries observed in recent years [16]. Consequently, there is an increasing need to analyze the biomechanical factors underlying these injuries, especially within the context of frequently used techniques such as the Roundhouse kick.

Previous studies on Taekwondo-related injuries have predominantly employed epidemiological methods, which offer valuable insights into injury prevalence and distribution. For example, Park et al. [17]found that 65.5% of injuries occurred in the lower limbs, with the knee being one of the most affected regions. Zhu [18] and Ji [19] similarly reported that knee injuries account for 30–40% of all cases. These injuries often result from high impact kicking actions and include ligament sprains, meniscal tears, and muscular strains. However, these studies largely focus on statistical descriptions and lack in-depth biomechanical analysis, particularly in relation to specific high-risk movements.

Although a limited number of recent studies have utilized finite element modeling to investigate stress distribution in knee tissues during Taekwondo techniques[20],[21], the integration of experimental kinematic data with simulation models remains underdeveloped. Furthermore, existing biomechanical studies rarely isolate the Roundhouse kick as a distinct movement for analysis, despite its strategic importance and mechanical intensity. This study aims to address these limitations by combining motion capture, force platform measurements, and finite element analysis to examine the mechanical loading experienced by knee ligaments and menisci during the execution of the Roundhouse kick. The findings are intended to improve our understanding of knee tissue mechanical loading and stress distribution

during the Roundhouse kick in elite male Taekwondo athletes and to inform population-specific prevention strategies.

Methods

Subjects

This study used G*Power (v3.1.9.2, Heinrich-Heine University, Düsseldorf, Germany) to estimate the required sample size. Assuming a large effect size (0.8), the power analysis indicated that a minimum of 12 participants would be needed to achieve 80% power at an alpha level of 0.05 [5]. To account for potential attrition, 14 elite male Taekwondo athletes (all competitive level ≥ 2) were recruited from the Taekwondo training team of Wuhan Sports University. All participants had trained continuously for more than three years (training history: 3.8 ± 2.0 years), with a routine training schedule of 5 days per week and approximately 3 hours per day. To reduce sex-related biomechanical variability, only male athletes were included. Participants self-reported no lower-limb injuries within the past 6 months and avoided high-intensity training during the 24 hours prior to testing. Leg dominance was determined based on self-reported preferred kicking leg; in this experiment, the attacking leg was defined as the kicking leg and the supporting leg as the stance leg. After excluding two athletes who were unable to complete the experimental protocol, data from 12 athletes (age: 17.79 ± 2.26 years; height: 181.93 ± 8.32 cm; body mass: 69.36 ± 14.44 kg) were included in the final analysis.

This study was approved by the Ethics Committee of Wuhan Sports University (Approval No.: 2022048). All methods were performed in accordance with the relevant institutional guidelines and regulations and complied with the principles of the Declaration of Helsinki. Written informed consent was obtained from all participants prior to participation. For participants under 18 years of age, written informed consent was obtained from their parents or legal guardians, and written assent was obtained from the participants themselves.

Data Collection

Ten T40 motion-capture cameras (T40, Vicon, UK; sampling frequency 200 Hz) were ceiling-mounted in a linear array along the long side of the lab (see site photos). Adjacent cameras formed 45°–90° viewing angles to create overlapping volumes over the striking workspace and reduce occlusion. The system operated at 200 Hz. Dynamic wand calibration and static L-frame calibration were performed daily, followed by a T-pose acquisition for model scaling and anatomical registration. During data collection, reprojection error was monitored in real time (target < 1 mm), with camera adjustments or gap-filling applied when necessary.

Four Kistler 3-D force plates (9260AA6, Switzerland; sampling frequency 1000 Hz; each 60 × 40 cm) were flush-mounted in the floor and arranged as a 2 × 2 matrix at the center of the testing area; their positions and orientations

were registered to the global laboratory coordinate system (see blue area in the schematic). Foot-contact events were identified using a vertical GRF threshold (Fz, **N**; threshold = **10 N**) in combination with marker-based events to segment task phases.

A Noraxon wireless surface EMG system (USA; sampling frequency 2000 Hz) was used. Skin was prepared according to SENIAM recommendations (shaving, alcohol cleaning, light abrasion). Bipolar Ag/AgCl electrodes were placed along the muscle fiber direction over the muscle belly with an inter-electrode distance ≈ 20 mm; The reference electrode was placed over a bony prominence. Each channel was verified by brief functional contractions to confirm signal quality and check for potential crosstalk.

A Daedo electronic protector system (trunk and headgear; four transmitters, one receiver, and a scoring computer) served as the striking target and adjudication device, recording valid hits and impact intensity in real time. A single experienced coach evaluated trial quality against competition technical standards to ensure technical consistency.

Vicon and Kistler were hardware-synchronized via a digital acquisition converter (Vicon provided the master trigger). The EMG system received start/stop triggers via trigger lines and port commands, achieving frame-level time alignment across all three systems. For each recording block, a “sync zipper test” was performed—tapping the force plate while moving a marker wand within the camera field and triggering EMG—to verify timestamp consistency. If a fixed delay or minor drift was detected, a time-offset correction was applied at export or during preprocessing.

EMG processing and EMG–OpenSim comparison

Raw EMG signals (sampling frequency 2000 Hz) were processed in MATLAB. Signals were demeaned and band-pass filtered (20–450 Hz, 4th-order, zero-lag Butterworth). When necessary, a notch filter was applied at the local power-line frequency to reduce electrical interference. The filtered signals were full-wave rectified and then low-pass filtered to obtain linear envelopes (4th-order, zero-lag Butterworth; cutoff frequency = 6 Hz, applied consistently across all muscles). For each muscle and participant, EMG linear envelopes were amplitude-normalized to a reference value defined consistently across trials (e.g., the peak value observed across all analyzed kick trials for that muscle). EMG and motion-capture/force-plate signals were synchronized by the acquisition system and time-aligned using the same event definitions used for kinematic/kinetic segmentation. The EMG linear envelopes were then resampled to match the kinematic time base and time-normalized to 0–100% of the movement cycle for averaging. OpenSim muscle activations were processed using the same time-normalization, enabling waveform-to-waveform comparisons. Agreement between OpenSim-estimated activations and normalized EMG linear envelopes was quantified using Pearson correlation coefficients (r) computed across the time-normalized waveform; 95% confidence intervals were estimated using a standard Fisher

z transformation.

Movement Phases

The biomechanical execution of the Roundhouse kick involves a sequence of complex joint actions, including ankle plantarflexion, hip flexion, and rapid knee extension, which are essential for generating striking velocity and impact force [22]. Given the “fast strike and faster retraction” characteristic of this technique [6], and drawing on prior literature [7][8][23] as well as interviews with elite Taekwondo coaches and athletes, we defined four key biomechanical moments (E1–E4) and three phases (P1–P3) to represent the temporal structure of the kick. To ensure biomechanical justification and repeatability, the following definitions were used (illustrated in Figure 1):

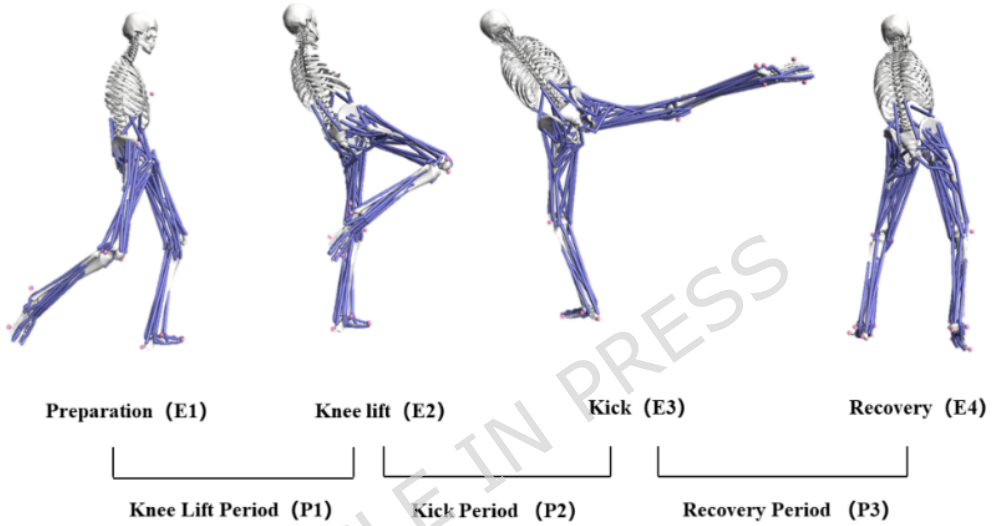

Figure 1. Schematic diagram of the Roundhouse kick movement phases

Preparation Moment (E1): Defined as the instant the attacking leg leaves the force platform, indicated when the vertical GRF under the attacking foot drops below the contact threshold ($Fz \geq 10$ N). This marks the initiation of the airborne phase. Knee Lift Moment (E2): Defined as the instant the attacking leg reaches maximum knee flexion angle during the flight, a key preparatory action for energy storage via the stretch-shortening cycle. Kick Moment (E3): Defined as the instant the knee achieves maximum extension angular velocity, just before impact, capturing the peak force transmission potential. Recovery Moment (E4): Defined as the instant the attacking foot contacts the force platform again, indicated when the vertical GRF rises above the same threshold ($Fz \leq 10$ N). Correspondingly, we define three motion phases: Knee lift period (P1): From toe-off (E1) to peak knee flexion (E2), representing loading and angular acceleration. Kicking Phase (P2): From peak knee flexion (E2) to peak knee extension (E3), representing the primary power generation stage. Recovery Phase (P3): From peak extension (E3) to ground contact (E4), representing recovery and stabilization.

OpenSim Model Construction and Knee Joint Loading

This study used OpenSim software to calculate the knee joint loads during

the Roundhouse kick. The Gait2392_Simbody model from the OpenSim model library was selected, which features two degrees of freedom (DOF) for knee flexion/extension [24]. Since the biomechanical characteristics of knee joint injuries were the focus of this study, a 6DOF (six degrees of freedom) musculoskeletal model of the knee joint was developed for simulation.

Data from three trials per subject were selected for musculoskeletal model simulation. To integrate experimental motion/force data with finite element analysis while keeping the modelling tractable, we adopted a single reference knee geometry (see next section) and applied group-averaged kinematics and kinetics from the cohort as loading inputs. OpenSim software was used for model scaling, inverse kinematics, residual reduction, static optimization, and joint reaction analysis to compute knee joint angles. The joint angle and moment data were filtered using a zero-lag fourth-order Butterworth low-pass filter in Matlab R2019a, with cutoff frequencies of 6 Hz and 10 Hz, respectively [25],[26]. The mean (±SD) knee joint angles and joint forces/moments across the 12 subjects were computed at the four key moments, and the mean values were used as boundary conditions for finite element analysis (Table 1). This approach was intended to examine qualitative stress-distribution patterns and relative differences between phases and between the supporting and attacking legs, rather than predict subject-specific absolute stresses.

The mean (±SD) knee joint angles and joint forces/moments across the 12 subjects were computed at the four key moments, and the mean values were used as boundary conditions for the finite element simulations (Table 1). In the present study, FE simulations were conducted only at these four key moments using the cohort-mean loading conditions; separate FE simulations were not performed for each individual subject or for each trial. Therefore, the FE results are presented descriptively to highlight qualitative stress-distribution patterns and relative differences under the modelling assumptions, rather than as group-level statistical outcomes. The standard deviations in Table 1 are provided to reflect between-subject variability in the input kinematics/kinetics, but variability in FE outputs was not quantified statistically. Individual muscle forces were not applied as separate loads in the finite element (FE) model. Instead, the FE boundary conditions were defined using the net knee joint reactions (resultant forces [N] and moments [N·m], where available) obtained from OpenSim joint reaction analysis. These net joint reactions represent the combined effect of muscle forces, external forces (e.g., ground reaction), and inertial effects transmitted across the joint. Accordingly, statistical inference in this study pertains to experimental kinematic/kinetic variables (Table 1 inputs), whereas FE outputs are used to illustrate comparative stress-distribution patterns under consistent modelling assumptions.

In the present FE framework, individual muscle forces were not applied explicitly as separate loads at anatomical attachment sites. Instead, the FE boundary conditions were driven by the resultant knee joint reactions (forces

and moments) obtained from OpenSim, which represent the combined effect of muscle forces, external forces, and inertial effects transmitted across the joint. This approach is intended to characterize global joint-level mechanical loading consistently across key moments; however, it does not resolve muscle-specific contributions or stabilization effects (e.g., quadriceps–hamstrings co-contraction) that may influence ligament load sharing and the absolute magnitude of ligament stresses.

Table 1. Group-mean knee joint angles and joint reaction forces at the four key moments (E1–E4) of the Roundhouse kick

Indicator		Preparation Moment (E1)			Knee Lift Moment (E2)			Kick Moment (E3)			Recovery Moment (E4)		
		X	Y	Z	X	Y	Z	X	Y	Z	X	Y	Z
Attacking Leg	Joint Angle	-74.45±3.21	-5.06±2.75	5.31±1.88	-122.01±4.02	5.24±2.31	7.72±3.65	-30.72±1.96	2.21±3.44	-5.42±2.02	-39.63±3.53	-28.64±1.85	6.74±2.67
	Joint Force	-1080.88±3.67	285.05±2.91	-344.85±2.14	-940.38±3.52	543.83±3.98	135.28±2.47	52.18±1.76	889.98±4.17	-42.47±3.11	-737.76±2.90	30.10±3.20	397.23±1.97
Supporting Leg	Joint Angle	-45.01±2.14	-18.43±3.33	8.24±1.97	-33.38±3.10	-5.92±2.42	9.39±3.55	-37.44±2.01	-14.95±1.69	8.01±3.04	-32.72±2.78	-13.22±3.31	9.97±2.23
	Joint Force	-986.64±3.24	46.50±2.08	155.70±3.36	-381.69±2.91	-58.94±1.99	749.39±4.12	604.71±3.42	-84.48±2.55	632.12±3.00	729.73±2.10	-306.49±3.77	802.89±2.35

Note: Joint angle unit (°); Joint force unit (N).

Agreement assessment between OpenSim-estimated muscle activations and normalized EMG linear envelopes

The normalized EMG linear envelopes were derived using the standardized preprocessing pipeline described in the Methods (filtering, rectification, linear envelope extraction, normalization, and time alignment/time normalization). To quantify agreement between EMG and model outputs, the processed EMG linear envelope and the corresponding OpenSim activation for each muscle were time-normalized to 0–100% of the kick cycle and resampled to 101 points; both signals were amplitude-normalized to their within-cycle maxima. Pearson correlation coefficients (r) were then computed over the full normalized time course, and 95% confidence intervals (CI) were obtained using Fisher's z transformation (N = 101). We interpreted $r \geq 0.75$ as strong agreement, $0.50 \leq r < 0.75$ as moderate agreement, and $r < 0.50$ as weak agreement; $r \geq 0.50$ was considered acceptable temporal agreement for supporting model use. Model validation

showed moderate-to-strong agreement across all muscles (r = 0.586–0.963; all 95% CIs excluded zero; see Fig. 2 and Table 2). The highest agreement was observed for the biceps femoris long head (BF) (r = 0.963, 95% CI 0.945–0.975). Gluteus maximus (GMAX) (r = 0.827, 95% CI 0.752–0.881) and lateral gastrocnemius (LG) (r = 0.812, 95% CI 0.733–0.870) also showed strong correlations, whereas medial gastrocnemius (MG) (r = 0.619, 95% CI 0.480–0.728), semimembranosus (SEM) (r = 0.607, 95% CI 0.465–0.718), and vastus lateralis (VL) (r = 0.586, 95% CI 0.439–0.702) exhibited moderate correlations. Taken together with the qualitative waveform comparisons, these results indicate that the model captures the main timing features of muscle activation and provides an acceptable match in relative amplitude trends for this movement, supporting its use in the subsequent comparative analyses.

Although the overall EMG–OpenSim agreement was high, three muscles (MG, SEM, and VL) showed only moderate correlations (r = 0.58–0.65), indicating that the model may not fully capture the amplitude and/or timing of activation bursts for all muscles during the rapid kicking task. This is plausible given known limitations of surface EMG in fast, high-acceleration movements (e.g., motion artefacts, sensitivity to electrode placement, and potential crosstalk), as well as modelling simplifications in OpenSim (e.g., generic muscle–tendon parameters and static-optimization assumptions that may not reproduce individual co-contraction strategies). Importantly, the FE boundary conditions in this study were imposed as cohort-mean net joint reactions (resultant joint loading) rather than individual muscle forces; therefore, these moderate discrepancies primarily limit muscle-specific interpretations and absolute stress magnitudes. Accordingly, the FE outputs are interpreted mainly in a comparative sense, focusing on relative stress-distribution patterns across key moments and between supporting and attacking legs under consistent modelling assumptions.

Table 2. Pearson correlation coefficients (r) between time-normalized (0–100% kick cycle, 101 points) OpenSim-estimated muscle activations and normalized EMG linear envelopes; 95% confidence intervals were calculated using Fisher's z transformation.

Muscle	r	95%CI
Biceps femoris, BF	0.963	0.945 – 0.975
Gluteus maximus, GMAX	0.827	0.752 – 0.881
Lateral gastrocnemius, LG	0.812	0.733 – 0.870
Medial gastrocnemius, MG	0.619	0.480 – 0.728
Semimembranosus, SEM	0.607	0.465 – 0.718
Vastus lateralis, VL	0.586	0.439 – 0.702

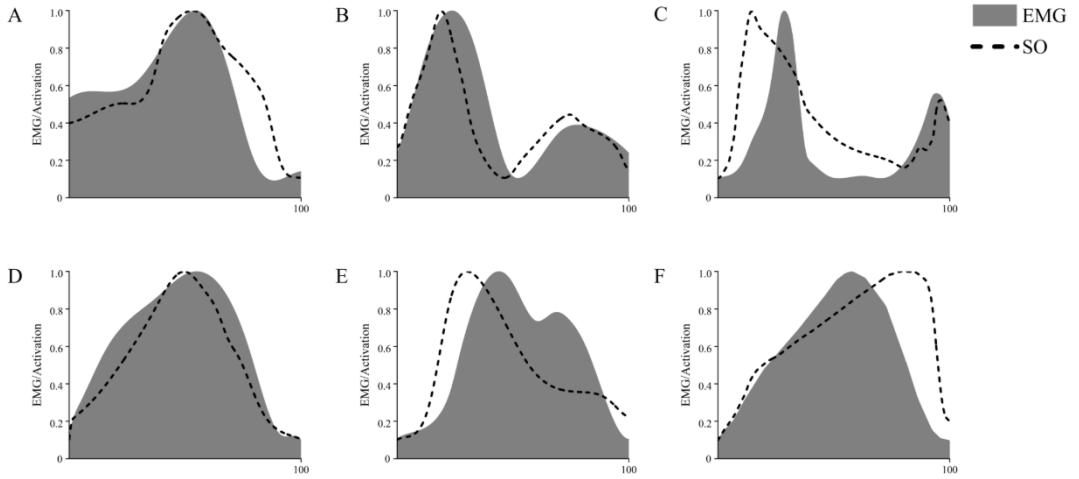

Figure 2. Comparison between OpenSim-estimated muscle activations (static optimization, dashed line) and normalized EMG linear envelopes (shaded area) over the normalized Roundhouse kick cycle (0–100%). Both EMG and OpenSim signals were time-normalized to 0–100% of the kick cycle and amplitude-normalized to their within-cycle maxima. Panels A–F correspond to biceps femoris long head (BF), lateral gastrocnemius (LG), gluteus maximus (GMAX), medial gastrocnemius (MG), semimembranosus (SEM), and vastus lateralis (VL), respectively.

Knee Joint Finite Element Model Construction

A single athlete whose height and body mass were closest to the cohort mean was selected to provide a reference knee geometry for the finite element model. CT and MRI data were acquired using a 64-slice multidetector CT scanner (GE Lightspeed VCT, USA) and a Siemens MAGNETOM Verio 3.0T superconducting MRI scanner (Germany) at Hubei Cancer Hospital. The scan was 0.625 mm, covering from the sole of the foot to 10 cm above the knee joint, and the data were saved in DICOM format. Accordingly, the FE outputs reported in this study represent descriptive mechanical loading patterns for this single knee geometry driven by cohort-mean boundary conditions and are interpreted primarily in a comparative sense rather than as population-level predictions.

Using Mimics 20.0 software, the CT and MRI data were imported to obtain knee joint images in the coronal, sagittal, and axial planes. The spatial positions of the anterior-posterior, medial-lateral, and superior-inferior directions were determined for each image. Based on the grayscale differences between bone and soft tissue, appropriate grayscale thresholds were set for image segmentation, preliminarily distinguishing bone and soft tissue. The integrity of bone images in different regions was ensured, and a preliminary 3D model of the knee joint was established.

The region-growing function in Mimics 20.0 was used for fine segmentation, identifying different bone structures. Mask editing was performed on each CT image layer, and the smoothing function was applied to

refine the surfaces of the femur, tibia, fibula, and patella. The final 3D model was exported in STL format. The STL files were imported into Geomagic Wrap software for mesh repair and optimization, including triangle deletion, smoothing, hole filling, and patching.

After model repair, simplification was performed to refine the mesh without altering the basic surface structure. Polygon processing was followed by shape processing to create an ideal surface model. Contour lines were detected and edited to form surface patches, which were then relaxed and adjusted to achieve smooth curves and uniform quadrilateral mesh sizes. The final model was saved in STEP format.

The STEP file was imported into SolidWorks to create a 3D model for further modification and assembly. The assembled knee joint model was then imported into HyperMesh 14.0 for finite element pre-processing, including mesh generation, material and property assignment, boundary condition application, and analysis step setup. Post-processing was performed in Abaqus software. The complete knee joint model is shown in Figure 3.

Material constitutive assumptions.

Tissue stresses were evaluated as the von Mises equivalent stress (S, Mises; MPa) in Abaqus. For each ligament and meniscus at each key moment, the reported “peak stress” was extracted as the maximum integration-point von Mises stress among all elements within the corresponding tissue volume (i.e., a local maximum rather than an element-averaged value). Because local maxima may be sensitive to stress concentration at attachment regions, mesh density, and simplified material assumptions (homogeneous linear-elastic isotropic properties without ligament pre-strain), absolute peak magnitudes should be interpreted cautiously. Therefore, the FE outputs are primarily used to describe relative mechanical loading patterns and spatial stress distributions across key moments and between legs under consistent modelling assumptions.

In this model, bone, articular cartilage, menisci, and major ligaments were all treated as homogeneous, linear elastic, isotropic materials, characterized by an elastic modulus and Poisson’s ratio (Table 3). This approach is a practical simplification to ensure numerical stability and computational feasibility given the limited availability of subject-specific nonlinear/anisotropic parameters. Consequently, the absolute magnitudes of tissue stress should be interpreted cautiously, and the FE results are primarily intended to support comparative interpretation (i.e., relative differences in stress distribution and loading trends across moments, legs, and tissues) under consistent modelling assumptions.

All FE simulations were performed at four discrete key moments (E1–E4) using cohort-mean kinematics/kinetics as inputs (Table 1). The tibia-based anatomical coordinate system was defined as X: medial–lateral (left–right), Y: superior–inferior (up–down), and Z: anterior–posterior (front–back). The joint angles and joint reaction forces reported in Table 1 were expressed in this

coordinate system; when OpenSim outputs were provided in a different reference frame, they were transformed to the FE anatomical coordinate system prior to application. The distal cut surfaces of the tibia (and fibula, if included) were fully constrained (all translational and rotational degrees of freedom fixed) to represent ground support and to prevent rigid-body motion. A reference point (RP) was created at a predefined location on the femoral shaft and kinematically coupled to the proximal femur nodes using a distributing coupling constraint. For each key moment, the prescribed joint rotations from Table 1 were applied at the RP to impose the joint posture, and the 3D joint reaction force vector from Table 1 was applied at the same RP as a concentrated load. All key-moment simulations were solved as quasi-static analyses under identical contact and material assumptions.

Hexahedral elements were employed for meshing bones and cartilage. The mesh sizes were selected to balance computational efficiency and accuracy, guided by established methodologies in the literature [27]-[30]. Specifically, a 1 mm mesh size was applied to the femur, tibia, fibula, and patella, while a finer mesh size of 0.5 mm was used for the menisci, femoral cartilage, and ligaments to accurately capture their complex geometries and mechanical behaviors. These mesh sizes have been validated in prior biomechanical finite element analyses, ensuring solution convergence and accuracy without undue computational cost. The material parameters and element properties ensured that the mechanical behaviors of bone, cartilage, menisci, and ligaments were reasonably simulated. Detailed parameters and properties are listed in Table 3.

Ligament pre-strain was not included in the present FE model. All ligaments were assumed to be stress-free in the reference configuration, and ligament stresses reported in this study were generated solely by the applied boundary conditions at the analyzed key moments. Because in vivo ligaments are typically pre-tensioned, omitting pre-strain may affect the absolute magnitudes of ligament stress and the relative ranking of which ligament appears most loaded; therefore, ligament stress values should be interpreted cautiously and mainly in a comparative sense under consistent modelling assumptions. Although the Roundhouse kick is a rapid movement, the present FE analysis was intentionally implemented as quasi-static key-moment snapshots to compare relative stress distributions at representative instants while avoiding uncertain inertial terms and subject-specific rate-dependent soft-tissue parameters. Accordingly, temporal dynamics (e.g., inertia, viscoelasticity, and strain-rate effects) were not modeled, and the FE results should be interpreted as comparative loading patterns under consistent assumptions.

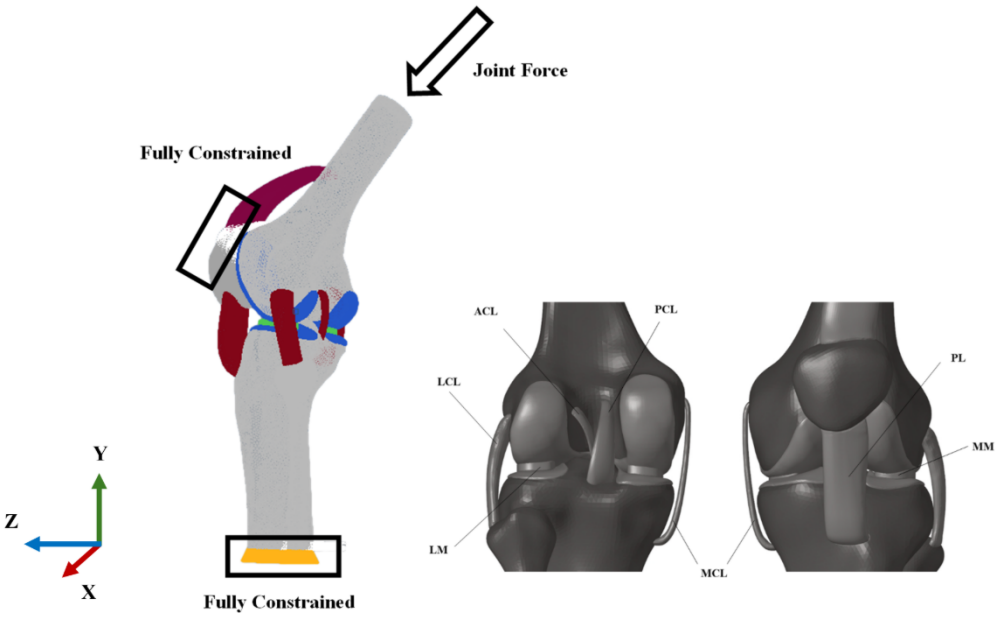

Figure 3. Finite element knee joint model with loading, boundary conditions, and anatomical coordinate system. The distal tibia (including the fibula) was fully constrained (all translational and rotational degrees of freedom fixed) to represent ground support and prevent rigid-body motion. A reference point (RP) was created on the femur and coupled to the proximal femoral nodes using a distributing coupling constraint. For each quasi-static key moment (E1–E4), prescribed joint rotations (joint angles) were applied at the RP to set the knee posture, and the 3D knee joint reaction force vector (Table 1) was applied at the same RP as a concentrated load.

Table 3. Material Parameters and Element Properties of the Finite Element Model

Tissue	Elastic Modulus (MPa)	Poisson's Ratio	Element Type
Bone	7300.00	0.30	Hexahedral
Femoral Cartilage	1.00	0.40	Hexahedral
Tibial Cartilage	1.00	0.40	Hexahedral
Meniscus	1.00	0.40	Hexahedral
Medial Collateral Ligament	332.00	0.49	Hexahedral
Lateral Collateral Ligament	345.00	0.49	Hexahedral
Anterior Cruciate Ligament	345.00	0.49	Hexahedral
Posterior Cruciate Ligament	345.00	0.49	Hexahedral
Patellar Ligament	345.00	0.49	Hexahedral

Validation of the Knee Joint Model

To evaluate whether the model can reproduce reasonable tibiofemoral contact behavior under a commonly used compressive benchmark condition, we performed a quasi-static axial-compression validation simulation. The distal tibia was fully constrained, and a 1000 N axial compressive load was applied to the femur along the superior–inferior direction via a coupled reference point (Fig. 4), consistent with previously published validation setups. Under the 1000 N load, the peak stress in the lateral meniscus was 4.57 MPa

(located at the anterior horn), the peak stress in the medial meniscus was 4.04 MPa (located at the lateral edge of the meniscal body near the anterior horn), the peak stress in the femoral cartilage was 1.17 MPa (in the contact region with the anterior horn of the lateral meniscus), and the peak stress on the tibial plateau was 4.20 MPa.

In addition, we compared the peak tibial plateau pressure and contact area against previously published knee finite element studies under the same 1000 N vertical loading condition (Fig. 5). Prior studies reported peak tibial plateau pressures of 2.39 MPa, 3.09 MPa, and 3.00 MPa, with total contact areas of 1015.8 mm^2, 1044.5 mm^2, and 1044.54 mm^2, respectively. Overall, these comparisons support that the contact-stress magnitudes and contact-area levels produced by the present model under a simplified axial-compression condition are comparable in order of magnitude[21][31][32]. Importantly, this validation is limited to a single axial-compression load case and does not directly validate the combined valgus, rotational, and shear loading conditions involved in the kick boundary conditions at E1–E4. Therefore, the stress results under the kick conditions are primarily intended for comparing relative distribution features and trend changes across key moments and between legs under consistent modelling assumptions.

Importantly, this validation is limited to a single axial-compression load case and therefore primarily supports the plausibility of tibiofemoral contact behavior (e.g., contact pressure/area and cartilage–meniscus stress magnitudes) under simplified loading. It does not provide a quantitative validation of ligament stress/strain responses, nor does it verify model predictions under the combined valgus, rotational, and shear loading conditions applied at E1–E4. Previous cadaveric and simulation studies have demonstrated that combined knee abduction/valgus moments and internal tibial rotation torques can markedly increase ACL strain, and that the MCL acts as a primary restraint under valgus loading [33]-[35]. Therefore, the ligament stress results reported in the present study should be interpreted mainly in a comparative sense (i.e., relative mechanical loading patterns across key moments and between legs) rather than as absolute predictors of ligament failure or injury risk.

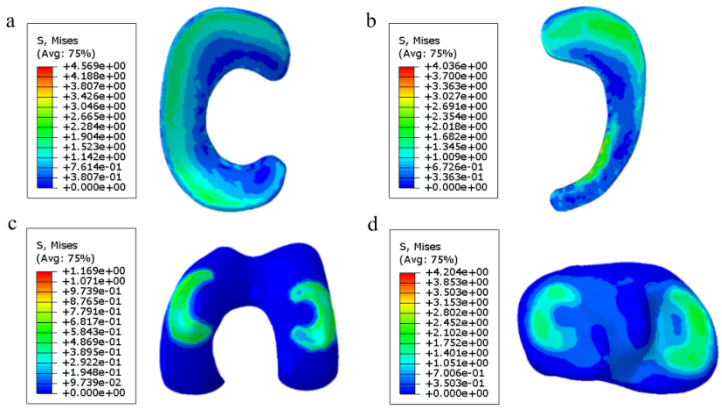

Figure 4. Von Mises stress contour maps under the 1000 N axial compression benchmark. A 1000 N compressive load was applied to the femur along the superior–inferior axis while the distal tibia was fully constrained (see Methods). Panels (a–d) show the lateral meniscus, medial meniscus, femoral cartilage, and tibia, respectively. Stress is reported in MPa; a color scale is provided in each subpanel.

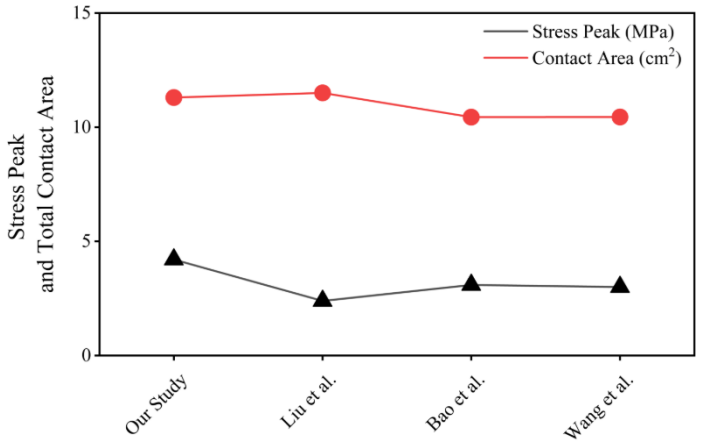

Figure 5. Comparison of peak tibial plateau contact pressure (MPa) and total contact area (cm²) under the 1000 N axial compression benchmark between the present model and previously published knee FE studies. Black triangles denote peak contact pressure, and red circles denote total contact area.

Results

Stress on Major Ligaments and Menisci of the Attacking Leg Knee Joint

All finite element results reported below are deterministic model outputs obtained from four quasi-static snapshots (E1–E4) under cohort-mean boundary conditions. Therefore, FE stress variables are presented descriptively to highlight relative loading/stress-distribution patterns rather than subjected to inferential statistical analysis. The corresponding stress contour maps are presented in Figures 6 (attacking leg) and 7 (supporting leg).

For the attacking leg knee, the ACL exhibited the highest stress at E2 (Knee Lift moment) with a peak value of 2.22 MPa, mainly concentrated near the femoral attachment region. ACL peak stress was 1.93 MPa at E1 and remained lower at E3 (1.61 MPa) and E4 (1.63 MPa). The PCL showed negligible stress across all four moments (peak ≈ 0 MPa). The MCL displayed its maximum stress at E3 (Kick moment) with a peak of 2.15 MPa, while the LCL stress remained low throughout the movement (peak ≤ 0.22 MPa). Regarding the menisci, the medial meniscus (MM) showed small but consistent stress exposure across moments with peak values around 0.56–0.59 MPa, whereas the lateral meniscus (LM) showed no noticeable stress (peak ≈ 0 MPa). Overall, stresses in the attacking leg were low and localized, indicating relatively limited mechanical loading under the applied cohort-mean boundary conditions (Figure 6).

Stress on Major Ligaments and Menisci of the Supporting Leg Knee Joint

In contrast, the supporting leg knee showed substantially higher stress exposure across most tissues. The ACL reached its maximum at E1 (Preparation moment) with a peak stress of 58.95 MPa, and remained high at E3 (53.78 MPa), with lower values at E2 (15.03 MPa) and E4 (26.79 MPa). The PCL demonstrated a similar trend, peaking at E1 (64.68 MPa) and E3 (62.96 MPa), followed by E4 (43.73 MPa) and E2 (15.05 MPa). The MCL showed its highest stress at E1 (15.66 MPa) and remained moderately loaded at E3 (11.75 MPa), with reduced stresses at E2 (8.07 MPa) and E4 (~5.05 MPa). The LCL exhibited minimal stress across all moments (peak ≤ 0.22 MPa). For the menisci, the MM peaked at E3 (4.56 MPa), while the LM showed the highest meniscal stress overall, peaking at E1 (6.64 MPa) and remaining elevated across the other moments (4.65–5.63 MPa). These results indicate that supporting leg experiences markedly greater mechanical loading (stress exposure) than the attacking leg at the analyzed key moments (Figure 7).

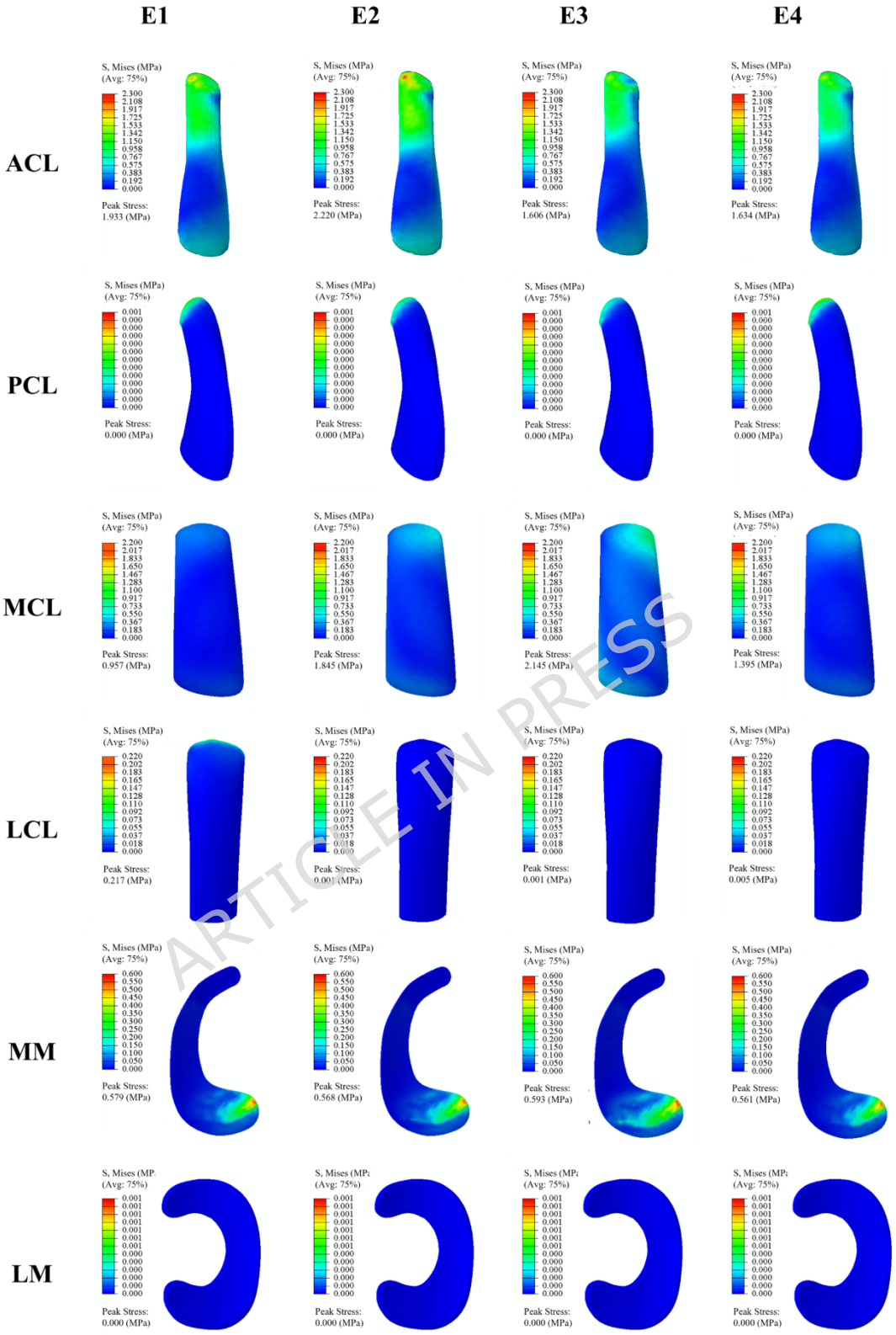

Figure 6. Von Mises stress distribution contour maps (MPa) of the major knee ligaments and menisci in the attacking leg at four key moments (E1–E4) of the Taekwondo Roundhouse kick (E1: Preparation; E2: Knee Lift; E3: Kick; E4: Recovery). For each tissue, the colour-bar limits are fixed across E1–E4 within the

attacking leg to enable consistent phase-wise visual comparison.

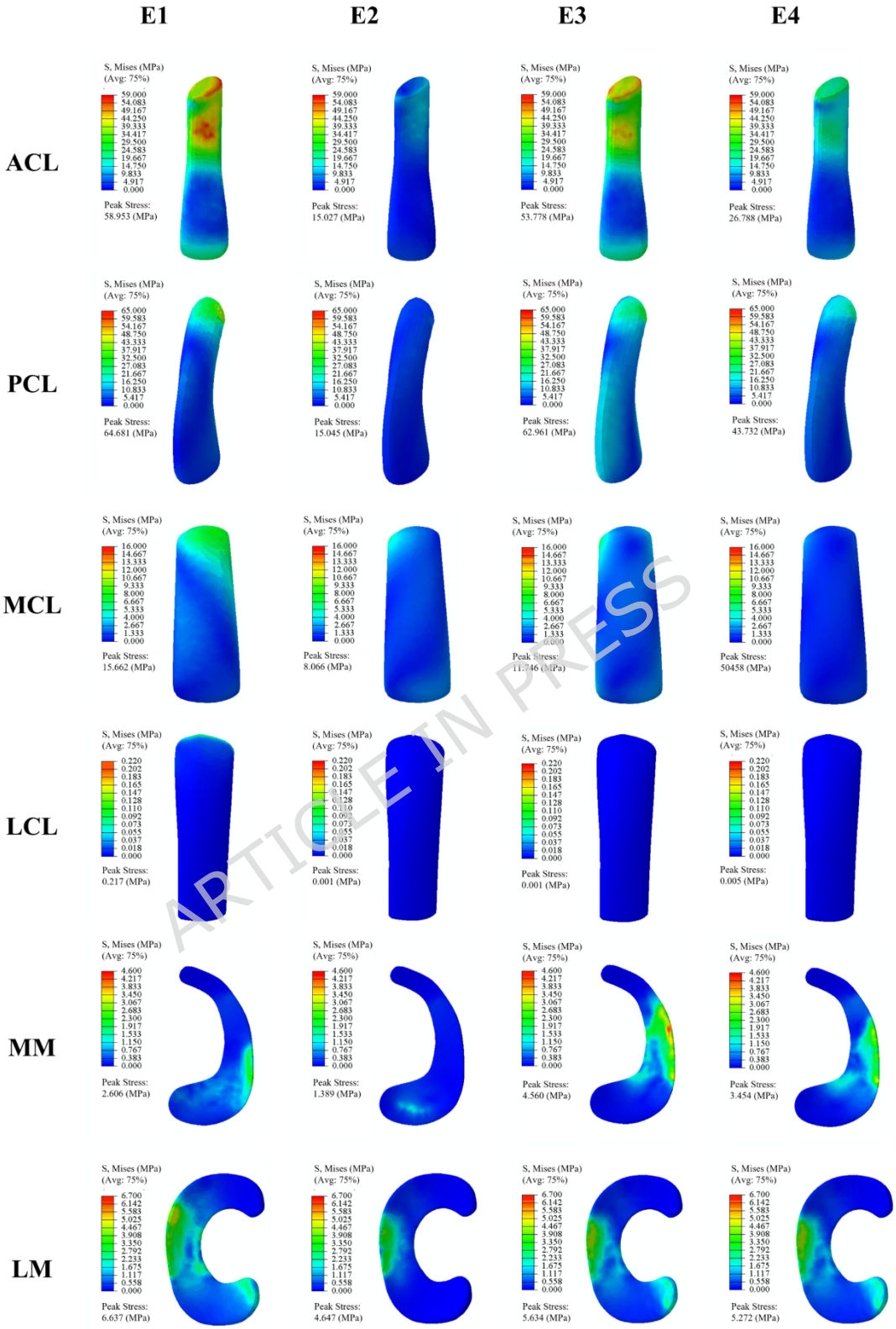

Figure 7. Von Mises stress distribution contour maps (MPa) of the major knee ligaments and menisci in the supporting leg at four key moments (E1–E4) of the Taekwondo Roundhouse kick (E1: Preparation; E2: Knee Lift; E3: Kick; E4:

Recovery).

Discussion

This study employed finite element analysis to investigate stress variations in the major ligaments and menisci of the knee joint during distinct phases of the Taekwondo Roundhouse kick. The results revealed clear biomechanical differences between the supporting and attacking legs, with higher peak stresses in the supporting leg across the analyzed structures, indicating greater mechanical loading (stress exposure) under the imposed boundary conditions rather than a quantitative prediction of injury probability.

The cruciate ligaments primarily function to stabilize the relative motion between the femur and tibia. During the transition from the Knee Lift Moment to the Kick Moment in the attacking leg, the knee approaches near full extension. The anterior cruciate ligament (ACL) works synergistically with the hamstrings to restrict anterior translation of the tibial plateau, thereby preventing anterior subluxation or dislocation of the tibia relative to the femur. Conversely, the posterior cruciate ligament (PCL) cooperates with the quadriceps to resist posterior translation of the tibial plateau, preventing posterior tibial displacement. Under deep flexion conditions, quadriceps engagement—alongside hamstring and ACL coordination—continues to limit anterior tibial movement.

In the current study, the attacking leg exhibited maximal knee flexion during the Knee Lift Moment, corresponding to the highest ACL stress, consistent with findings by Li et al. [36] , who reported that peak ACL stress coincides with maximum knee flexion. The ACL stress increased with greater knee flexion angles. However, this finding diverges from the results of Pan et al. [37], likely due to differences in boundary conditions across sport-specific biomechanical models.

According to Alentorn-Geli et al. [38], approximately 70% of cruciate ligament injuries are attributed to non-contact injuries. Dauty et al. [39] reported that the risk of cruciate ligament injury is associated with the maximum hip flexion angle, maximum knee valgus angle, maximum knee extension moment, maximum knee rotation moment, and the activation ratio of the quadriceps and hamstrings. During the preparation and striking moments, the foot of the supporting leg is fixed relative to the ground, and the rotation of the torso generates a significant internal torsional moment in the knee joint. Additionally, the supporting leg knee joint must rapidly extend to provide kinetic energy for hip rotation. Therefore, the extension moment, torsional moment, and body weight collectively contribute to greater cruciate-ligament mechanical loading in the supporting leg under the cohort-mean boundary conditions analyzed here. Prior experimental and epidemiological studies have linked combined rotational/valgus loading and near-extension postures with increased ACL strain and non-contact injury scenarios; thus, the loading pattern observed in our simulations may be relevant to proposed injury mechanisms [40]. However, the present FE analysis quantifies relative stress

distributions and does not define rupture thresholds or injury probabilities; any linkage to injury mechanisms should therefore be interpreted as an informed hypothesis rather than definitive evidence.

Regarding the menisci, the supporting leg's medial and lateral menisci showed peak stresses of 4.56 MPa and 6.64 MPa, respectively—markedly higher than the attacking leg (0.59 MPa and 0 MPa). Stress concentration was particularly evident at the peripheral body and posterior horn of the menisci, aligning with clinically common tear locations. Previous studies indicate that meniscal root tears typically occur under deep knee flexion and axial rotation [41],[42]. Circumferential collagen fibers in the meniscus normally distribute compressive loads to the periphery, maintaining even pressure distribution across the articular surface. Disruption of this mechanism—as in posterior root tears—alters knee biomechanics and may increase mechanical demand on the meniscus under combined compressive and torsional loading. Throughout the entire Roundhouse kick, the supporting knee experiences pronounced coronal and vertical axis torques along with joint reaction forces, producing elevated compressive and torsional loading on the menisci. The stress contour maps revealed higher stresses in the lateral meniscus compared to the medial meniscus, indicating greater mechanical loading on the lateral meniscus under the analyzed conditions. This observation aligns with findings from Xiang et al. and Jeon et al., who identified repetitive shear and torsional loads under weight-bearing conditions as key contributors to meniscal root loading/extrusion and degenerative changes [43],[44].

In terms of the collateral ligaments, the supporting leg’s medial collateral ligament (MCL) exhibited a peak stress of 15.66 MPa, primarily concentrated at its femoral attachment site. Although the lateral collateral ligament (LCL) showed a lower peak stress (0.22 MPa), it still bore measurable load during the Preparation and Knee Lift Moments. The MCL and LCL are crucial for maintaining frontal plane stability and controlling tibial rotation. The MCL is frequently injured alone or in conjunction with the ACL, while LCL injuries often co-occur with PCL tears [45]. Prior studies have examined the morphology and function of the collateral ligaments, noting that the LCL primarily resists varus forces across the range of knee flexion, while the MCL provides up to 80% of the resistance against valgus stress and also assists in limiting tibial external rotation and posterior translation [46]. During the Kick Moment, external impact forces on the attacking leg cause significant values loading on the MCL, resulting in peak stress near the femoral insertion. The fully extended posture at this phase may render the insertion site more vulnerable. Meanwhile, the supporting leg exhibited high MCL and LCL stresses throughout all four phases—likely due to its consistently near-extended posture and exposure to rotational and valgus loading. These biomechanical demands further explain the elevated risk of collateral ligament injury in the supporting leg. The MCL and LCL act as the primary resistors of frontal plane torques and help stabilize tibial rotation [47]. Accordingly, the observed high-

stress exposure in these ligaments underscores their critical role in load attenuation and suggests a significant risk of strain or rupture during repetitive high-intensity kicking tasks.

This study has several limitations. First, the FE simulations were performed using a single subject-specific knee geometry driven by cohort-mean boundary conditions, and therefore the stress magnitudes should be interpreted comparatively rather than as population-level predictions. Second, the FE analysis consisted of four independent quasi-static snapshots (E1–E4), which cannot fully capture transient dynamic effects during the rapid kicking motion. Third, ligament pre-strain and explicit muscle forces were not modelled, which may influence absolute ligament stress levels. Finally, only elite male athletes were included; thus, extrapolation to female athletes or other skill levels requires caution. Despite these limitations, the consistent supporting–attacking leg contrast across E1–E4 suggests robust relative mechanical loading patterns under the applied conditions.

Conclusion

The supporting leg consistently exhibited higher mechanical loading exposure across E1–E4 during the Roundhouse kick, with more pronounced and localized stress hotspots in the major ligaments and menisci. Ligament peak stresses were primarily concentrated near attachment regions, while meniscal high-stress areas were mainly located at the posterior horn and peripheral zones, with the supporting-leg lateral meniscus showing the most prominent stress concentration. Overall, the supporting knee carries the dominant mechanical demand during the Roundhouse kick, suggesting that training and technique optimization should prioritize load management of the supporting leg and control of stress exposure in key knee tissues.

List of abbreviations

Abbreviation	Full term (EN)
ACL	Anterior Cruciate Ligament
PCL	Posterior Cruciate Ligament
MCL	Medial Collateral Ligament
LCL	Lateral Collateral Ligament
PL	Patellar Ligament
MM	Medial Meniscus
LM	Lateral Meniscus
EMG	Electromyography
GRF	Ground Reaction Force
DOF	Degrees of Freedom
6DOF	Six Degrees of Freedom
FEA	Finite Element Analysis
MRI	Magnetic Resonance Imaging
CT	Computed Tomography
DICOM	Digital Imaging and Communications in Medicine
STL	Stereolithography File Format
STEP	Standard for the Exchange of Product Data
IOC	International Olympic Committee
WTF	World Taekwondo Federation (now World Taekwondo, WT)
BF	Biceps Femoris (long head)
GMAX	Gluteus Maximus
LG	Lateral Gastrocnemius
MG	Medial Gastrocnemius
SEM	Semimembranosus
VL	Vastus Lateralis
CI	Confidence Interval

Ethics approval and consent to participate

This study was approved by the Ethics Committee of Wuhan Sports University (Approval No.: 2022048). All procedures complied with relevant institutional requirements and local legislation. Written informed consent was obtained from all participants prior to data collection. No personally identifiable information was collected; all data was anonymized and securely stored with access restricted to authorized research team members.

Availability of data and materials

The raw data supporting the conclusion of this article will be made available by the authors, without undue reservation.

Competing interests

The authors declare that the research was conducted in the absence of any commercial or financial relationships that could be construed as a

potential conflict of interest.

Funding

The author(s) declared that financial support was received for the research, authorship, and/or publication of this article. This study was Joint supported by Hubei Provincial Natural Science Foundation and Sport Innovative Development of China (grant number 2025AFD652) and was supported by the East Lake Scholars Sponsorship Program of Wuhan Sports University in China (2023), Hubei Provincial Department of Education of China [grant number D20194101], the Hubei Provincial Department of Education Scientific Research Program for Young and Middle-aged Talents (grant number Q20224107), the Natural Science Basic Research Program of Shangxi Province [grant number 2022JQ-051], the Science and Technology Team Foundation of Wuhan Sports University [grant number 21KT02], and the 14th Five Year-Plan Advantageous and Characteristic Disciplines (Groups) of Colleges and Universities in Hubei Province [grant number 2021-05].

Author contributions

Mengyao Jia: Conceptualization, Data Management, Formal Analysis, Investigation, Methodology, Software, Supervision, Visualization, Writing - Original Draft, Writing - Review & Editing, Project Administration, Validation. Duo Li: Conceptualization, Methodology, Supervision, Writing - Review & Editing. Yong Ma: Funding Acquisition, Project Administration, Resources, Supervision, Writing - Review & Editing. Liu Lin: Investigation, Validation, Writing - Review & Editing. Lin Shijie: Funding Acquisition, Validation, Writing - Review & Editing. Huang Ruifeng: Data Management, Investigation, Validation, Writing - Review & Editing. Zhaoyi Wang: Investigation, Project Administration, Resources, Writing - Review & Editing. Zheng Weitao: Investigation, Data Management, Validation, Writing - Review & Editing. Xin Ji: Conceptualization, Methodology, Writing - Review & Editing.

References

[1] Zhang, N., & Guan, J. M. (2017). Technical and tactical characteristics of Taekwondo men's 58 kg champion Zhao Shuai at the 2016 Rio Olympics. *British journal of sports medicine*, 46(7), 485-491. https://doi.org/10.1136/bjsports-2012-091011

[2] Bridge, C. A., Ferreira da Silva Santos, J., Chaabene, H., Pieter, W., & Franchini, E. (2014). Physical and physiological profiles of taekwondo athletes. *Sports medicine*, 44, 713-733. https://doi.org/10.1007/s40279-014-0159-9

[3] Zhang, N., & Guan, J. M. (2017). Technical and Tactical Characteristics of Taekwondo Men's 58kg Champion Zhao Shuai in 2016 Rio Olympics. *Journal of Beijing Sport University*, 40(2): 95-99. DOI: 10.19582/j.cnki.11-3785/g8.2017.02.015

[4] Mailapalli, D. R., Benton, J., & Woodward, T. W. (2015). Biomechanics of the taekwondo axe kick: a review. *Journal of Human Sport and Exercise*, 10(1), 141-149. https://doi.org/10.14198/jhse.2015.101.12

[5] Hao, Y., Duan, H. J., & Ji, Z. Q. (2011). Biomechanics research on the offensive back

turning kick in long distance of elite Taekwondo players. *Journal of Beijing Sport University*, 34(4): 64-67. DOI: 10.19582/j.cnki.11-3785/g8.2011.04.017

[6] Yan, H. W., Shan, W., & Gao, Z. H. (2015). Technique application characteristics of main rivals of Chinese women Taekwondo athletes in 49 kg class. *Journal of Beijing Sport University*, 38(2): 112-116. DOI:10.19582/j.cnki.11-3785/g8.2015.02.019

[7] Su, J. J., Zhang, Y. H., Lu, Y., Wu, Z. H., Lei, T., Feng, C. H., & Li, Y. (2020). Covariate analysis of kinematic characteristics of Taekwondo athletes' ankle joints during turning kicks under different fatigue levels. *Chinese Journal of Sports Medicine*, 39(12): 924-931. DOI:10.16038/j.1000-6710.2020.12.002

[8] Xu, C. J., Liu, W. J., Liu, D. H., & Yu, H. L. (2020). Effect of hitting speed of four tactical movements of Taekwondo back roundhouse kick and its enlightenment for sports training. *Journal of Chengdu Sport University*, 46(1): 114-120. DOI: 10.15942/j.jcsu.2020.01.018

[9] Son, B., Cho, Y. J., Jeong, H. S., & Lee, S. Y. (2020). Injuries in Korean elite taekwondo athletes: A prospective study. *International journal of environmental research and public health*, 17(14), 5143. https://doi.org/10.3390/ijerph17145143

[10] Altarriba-Bartes, A., Drobnic, F., Til, L., Malliaropoulos, N., Montoro, J. B., & Irurtia, A. (2014). Epidemiology of injuries in elite taekwondo athletes: two Olympic periods cross-sectional retrospective study. *BMJ open*, 4(2), e004605. https://doi.org/10.1136/bmjopen-2013-004605

[11] Son, M., Youm, C., Woo, J., Lee, M., Kim, Y., & Kim, J. (2018). Postural stability for taekwondo athletes with repetitive ankle sprains during a single-leg stance. *Journal of physical therapy science*, 30(3), 405-410. https://doi.org/10.1589/jpts.30.405

[12] Xu, D., Zhou, H., Quan, W., Ma, X., Chon, T. E., Fernandez, J., ... & Gu, Y. (2024). New insights optimize landing strategies to reduce lower limb injury risk. Cyborg and Bionic Systems, 5, 0126. https://spj.science.org/doi/full/10.34133/cbsystems.0126

[13] Xu, D., Zhou, H., Quan, W., Gusztav, F., Wang, M., Baker, J. S., & Gu, Y. (2023). Accurately and effectively predict the ACL force: Utilizing biomechanical landing pattern before and after-fatigue. Computer Methods and Programs in Biomedicine, 241, 107761. https://doi.org/10.1016/j.cmpb.2023.107761

[14] Cristiani, R., van de Bunt, F., Kvist, J., & Stålman, A. (2023). High prevalence of meniscal ramp lesions in anterior cruciate ligament injuries. *Knee Surgery, Sports Traumatology, Arthroscopy*, 31(1), 316-324. https://doi.org/10.1007/s00167-022-07135-8

[15] Kim, Y. J., Kim, J. G., Chang, S. H., Shim, J. C., Kim, S. B., & Lee, M. Y. (2010). Posterior root tear of the medial meniscus in multiple knee ligament injuries. *The Knee*, 17(5), 324-328. https://doi.org/10.1016/j.knee.2009.10.001

[16] Falco, C., Alvarez, O., Castillo, I., Estevan, I., Martos, J., Mugarra, F., & Iradi, A. (2009). Influence of the distance in a roundhouse kick's execution time and impact force in Taekwondo. *Journal of biomechanics*, 42(3), 242-248. https://doi.org/10.1016/j.jbiomech.2008.10.041

[17] Park K J, Song B B. Injuries in female and male elite taekwondo athletes: a 10-year prospective, epidemiological study of 1466 injuries sustained during 250 000 training hours[J]. British Journal of Sports Medicine, 2018, 52(11): 735-740.

https://doi.org/10.1136/bjsports-2017-097530

[18] Zhu, L., & Gao, X. (2010). Clinical summary of conservative rehabilitation treatment for posterior cruciate ligament rupture in six Taekwondo athletes. Chinese Journal of Sports Medicine, (3), 2. DOI:10.16038/j.1000-6710.2010.03.022

[19] Ji M J. Analysis of injuries in taekwondo athletes[J]. Journal of Physical Therapy Science, 2016, 28(1): 231-234. https://doi.org/10.1589/jpts.28.231

[20] Sun, Y., Liu, L. S., & Ma, Y. C. (2024). Finite element analysis of internal knee joint stresses under different side-cut angles and ground contact modes. *Chinese Journal of Rehabilitation Medicine*, 39(10): 1449-1455+1461. DOI:10.3969/j.issn.1001-1242.2024.10.007

[21] Liu, L. S., Pan, Z. Y., Li, X. M., & Ma, Y. C. (2025). Analysis of knee joint stress characteristics under different touchdown methods during barefoot running. *Chinese Journal of Rehabilitation Medicine*, 40(1): 53-60. DOI:10.3969/j.issn.1001-1242.2025.01.009

[22] Gavagan, C. J., & Sayers, M. G. (2017). A biomechanical analysis of the roundhouse kicking technique of expert practitioners: A comparison between the martial arts disciplines of Muay Thai, Karate, and Taekwondo. *PloS one*, 12(8), e0182645. https://doi.org/10.1371/journal.pone.0182645

[23] Liu, L. S., Pan, Z. Y., Li, X. M., & Ma, Y. C. (2025). Analysis of knee joint stress characteristics under different touchdown methods during barefoot running. *Journal of Wuhan Sports University*, 57(1): 73-81. DOI: 10.15930/j.cnki.wtxb.2023.01.009

[24] Delp, S. L., Anderson, F. C., Arnold, A. S., Loan, P., Habib, A., John, C. T., ... & Thelen, D. G. (2007). OpenSim: open-source software to create and analyze dynamic simulations of movement. *IEEE transactions on biomedical engineering*, 54(11), 1940-1950. https://doi.org/10.1109/TBME.2007.901024

[25] Alexander, N., Schwameder, H., Baker, R., & Trinler, U. (2021). Effect of different walking speeds on joint and muscle force estimation using AnyBody and OpenSim. *Gait & posture*, 90, 197-203. https://doi.org/10.1016/j.gaitpost.2021.08.026

[26] Lu, Z., Li, X., Rong, M., Baker, J. S., & Gu, Y. (2022). Effect of rearfoot valgus on biomechanics during barbell squatting: A study based on OpenSim musculoskeletal modeling. *Frontiers in neurorobotics*, 16, 832005. https://doi.org/10.3389/fnbot.2022.832005

[27] Li, Y. L., Xu, Y., Chen, X. Y., & Ni, G. X. (2024). Effects of running fatigue on ankle biomechanics in runners with different levels of experience. *Chinese Journal of Rehabilitation Medicine*, 39(11): 1714-1717. DOI:10.3969/j.issn.1001-1242.2024.11.026

[28] Malige, A., Baghdadi, S., Hast, M. W., Schmidt, E. C., Shea, K. G., & Ganley, T. J. (2022). Biomechanical properties of common graft choices for anterior cruciate ligament reconstruction: a systematic review. *Clinical Biomechanics*, 95, 105636. https://doi.org/10.1016/j.clinbiomech.2022.105636

[29] Milinkovic, D. D., Fink, C., Kittl, C., Sillanpää, P., Herbst, E., Raschke, M. J., & Herbort, M. (2021). Anatomic and biomechanical properties of flat medial patellofemoral ligament reconstruction using an adductor magnus tendon graft: a human cadaveric study. *The American Journal of Sports Medicine*, 49(7), 1827-1838.

https://doi.org/10.1177/036354652110095

[30] Zhang, Y., Hao Z. X., Jin, D. W., & Sun, M. X. (2007). A method of vivo human knee joint 3D model reconstruction based on MR images. Chinese *Journal of Rehabilitation Medicine*, 22(4): 339-342.

[31] Bao, H. R. C., Zhu, D., Gong, H., & Gu, G. S. (2013). The effect of complete radial lateral meniscus posterior root tear on the knee contact mechanics: a finite element analysis. *Journal of Orthopaedic Science*, 18, 256-263. https://doi.org/10.1007/s00776-012-0334-5

[32] Wang, J. Y., Qi, Y. S., Bao, H. R. C., Xu, Y. S., Wei, B. G., Wang, Y. X., ... & Lv, F. (2021). The effects of different repair methods for a posterior root tear of the lateral meniscus on the biomechanics of the knee: a finite element analysis. *Journal of orthopaedic surgery and research*, 16(1), 296. https://doi.org/10.1186/s13018-021-02435-0

[33] Shin, C. S., Chaudhari, A. M., & Andriacchi, T. P. (2011). Valgus plus internal rotation moments increase anterior cruciate ligament strain more than either alone. *Medicine & Science in Sports & Exercise*, 43(8), 1484-1491. https://doi.org/10.1249/MSS.0B013E31820F8395

[34] Quatman, C. E., Kiapour, A. M., Demetropoulos, C. K., Kiapour, A., Wordeman, S. C., Levine, J. W., ... & Hewett, T. E. (2014). Preferential loading of the ACL compared with the MCL during landing: a novel in sim approach yields the multiplanar mechanism of dynamic valgus during ACL injuries. *The American journal of sports medicine*, *42*(1), 177-186. https://doi.org/10.1177/0363546513506558

[35] Oh, Y. K., Lipps, D. B., Ashton-Miller, J. A., & Wojtys, E. M. (2012). What strains the anterior cruciate ligament during a pivot landing?. *The American journal of sports medicine*, *40*(3), 574-583. https://doi.org/10.1177/0363546511432544

[36] Li, P. X., Zhao, G. P., Xia, F. Y., et al. (2020). Finite unicompartmental knee arthroplasty in ACL fracture of the knee joint. *Journal of Medical Biomechanics*, 35(1): 70-76. DOI: 10.16156/j.1004-7220.2020.01.015

[37] Pan, Z. Y., Ma, Y., Geng, Z. Z., et al. (2021). Finite element analysis on stress state of knee joint with different lateral cutting angles under expected conditions. *Journal of Medical Biomechanics*, 36(5): 762-768. DOI: 10.16156/j.1004-7220.2021.05.016

[38] Alentorn-Geli, E., Mendiguchía, J., Samuelsson, K., Musahl, V., Karlsson, J., Cugat, R., & Myer, G. D. (2014). Prevention of anterior cruciate ligament injuries in sports—Part I: Systematic review of risk factors in male athletes. *Knee surgery, sports traumatology, arthroscopy*, 22, 3-15. https://doi.org/10.1007/s00167-013-2725-3

[39] Dauty, M., Crenn, V., Louguet, B., Grondin, J., Menu, P., & Fouasson-Chailloux, A. (2022). Anatomical and neuromuscular factors associated to non-contact anterior cruciate ligament injury. *Journal of clinical medicine*, 11(5), 1402. https://doi.org/10.3390/jcm11051402

[40] Shin, C. S., Chaudhari, A. M., & Andriacchi, T. P. (2007). The influence of deceleration forces on ACL strain during single-leg landing: a simulation study. *Journal of biomechanics*, 40(5), 1145-1152. https://doi.org/10.1016/j.jbiomech.2006.05.004

[41] Floyd, E. R., Rodriguez, A. N., Falaas, K. L., Carlson, G. B., Chahla, J., Geeslin, A. G., & LaPrade, R. F. (2021). The natural history of medial meniscal root tears: a biomechanical and clinical case perspective. *Frontiers in Bioengineering and*

Biotechnology, 9, 744065. https://doi.org/10.3389/fbioe.2021.744065

[42] Willinger, L., Lang, J. J., von Deimling, C., Diermeier, T., Petersen, W., Imhoff, A. B., ... & Achtnich, A. (2020). Varus alignment increases medial meniscus extrusion and peak contact pressure: a biomechanical study. *Knee Surgery, Sports Traumatology, Arthroscopy*, 28, 1092-1098. https://doi.org/10.1007/s00167-019-05701-1

[43] Xiang, F. R., Tang, S. X., Liu, X. X., et al. (2023). Analysis of knee joint stress during drop jump landing in females with generalized joint hypermobility. *Journal of Medical Biomechanics*, 38(2): 317-323. DOI: 10.16156/j.1004-7220.2023.02.017

[44] Jeon, S. W., Jung, M., Choi, C. H., Kim, S. G., & Kim, S. H. (2021). Factors related to meniscal extrusion and cartilage lesions in medial meniscus root tears. *The Journal of Knee Surgery*, 34(02), 178-186. https://doi.org/10.1055/s-0039-1693708

[45] Elkin, J. L., Zamora, E., & Gallo, R. A. (2019). Combined anterior cruciate ligament and medial collateral ligament knee injuries: anatomy, diagnosis, management recommendations, and return to sport. *Current Reviews in Musculoskeletal Medicine*, 12, 239-244. https://doi.org/10.1007/s12178-019-09549-3

[46] Wilson, W. T., Deakin, A. H., Payne, A. P., Picard, F., & Wearing, S. C. (2012). Comparative analysis of the structural properties of the collateral ligaments of the human knee. *Journal of orthopaedic & sports physical therapy*, 42(4), 345-351. https://www.jospt.org/doi/10.2519/jospt.2012.3919

[47] Ren, D., Liu, Y., Zhang, X., Song, Z., Lu, J., & Wang, P. (2017). The evaluation of the role of medial collateral ligament maintaining knee stability by a finite element analysis. *Journal of orthopaedic surgery and research*, 12, 1-10. https://doi.org/10.1186/s13018-017-0566-3

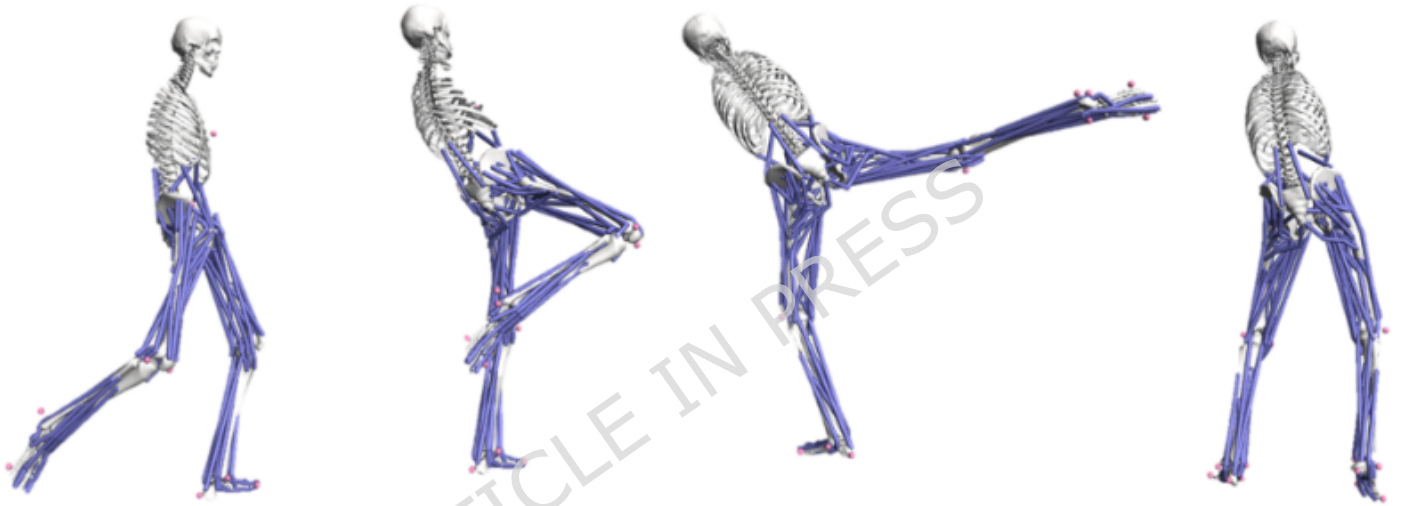

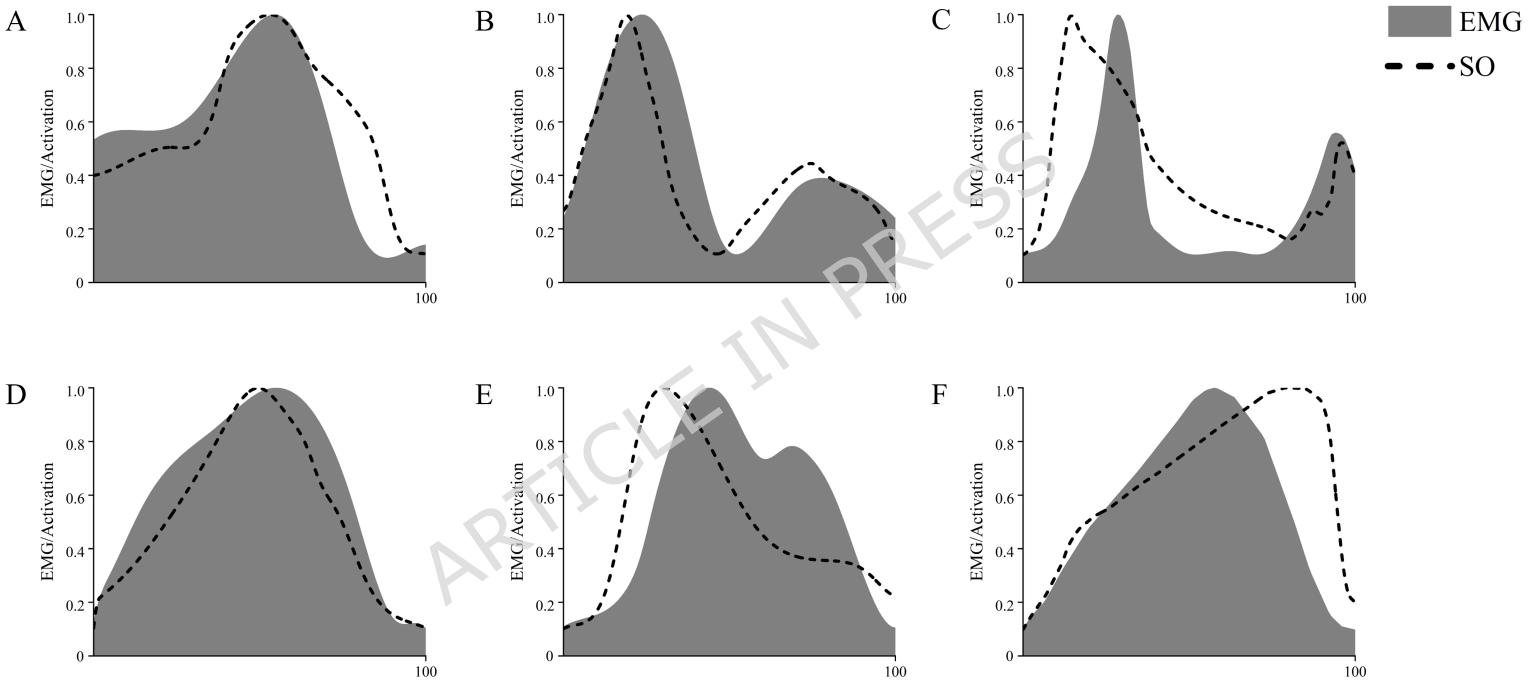

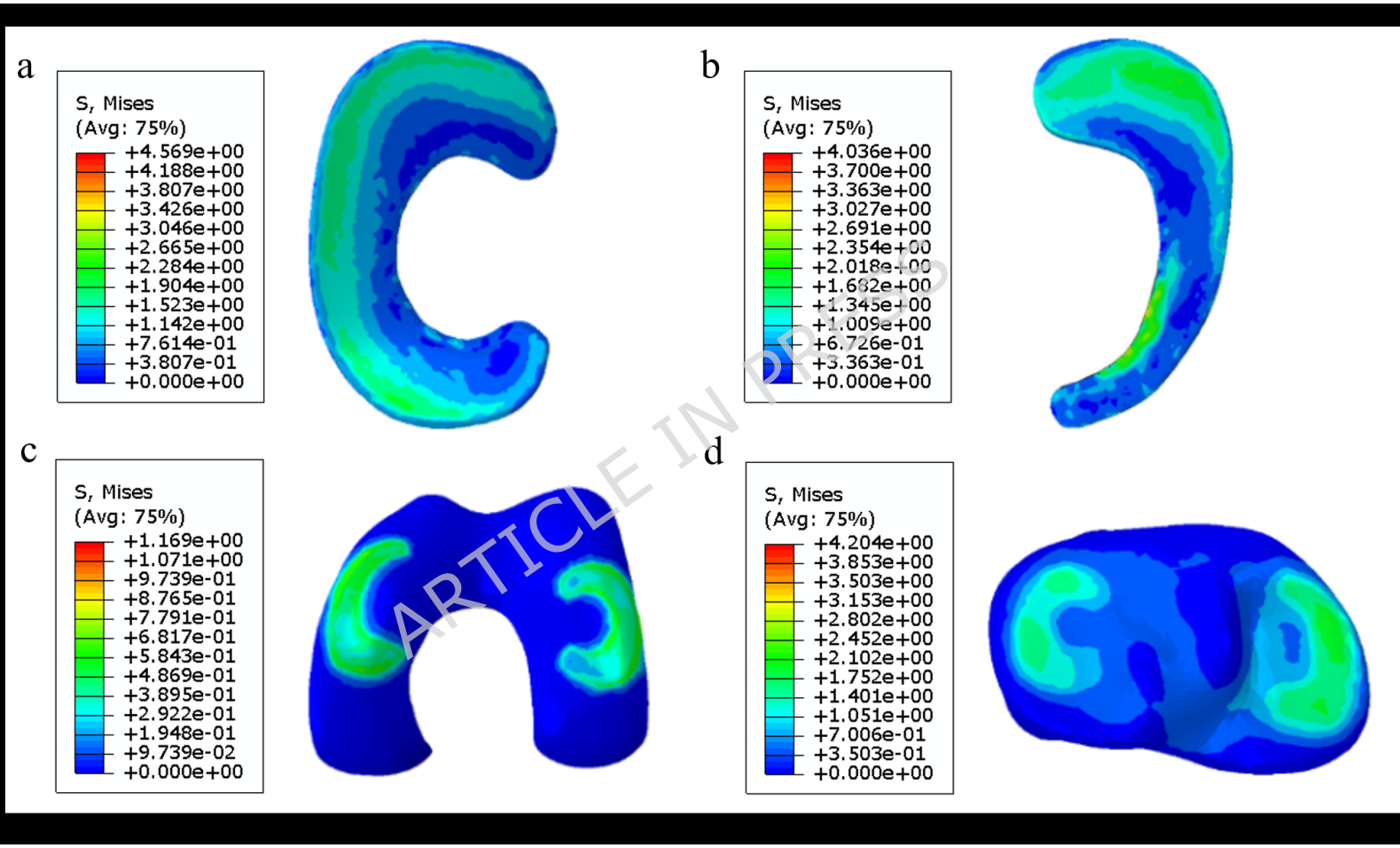

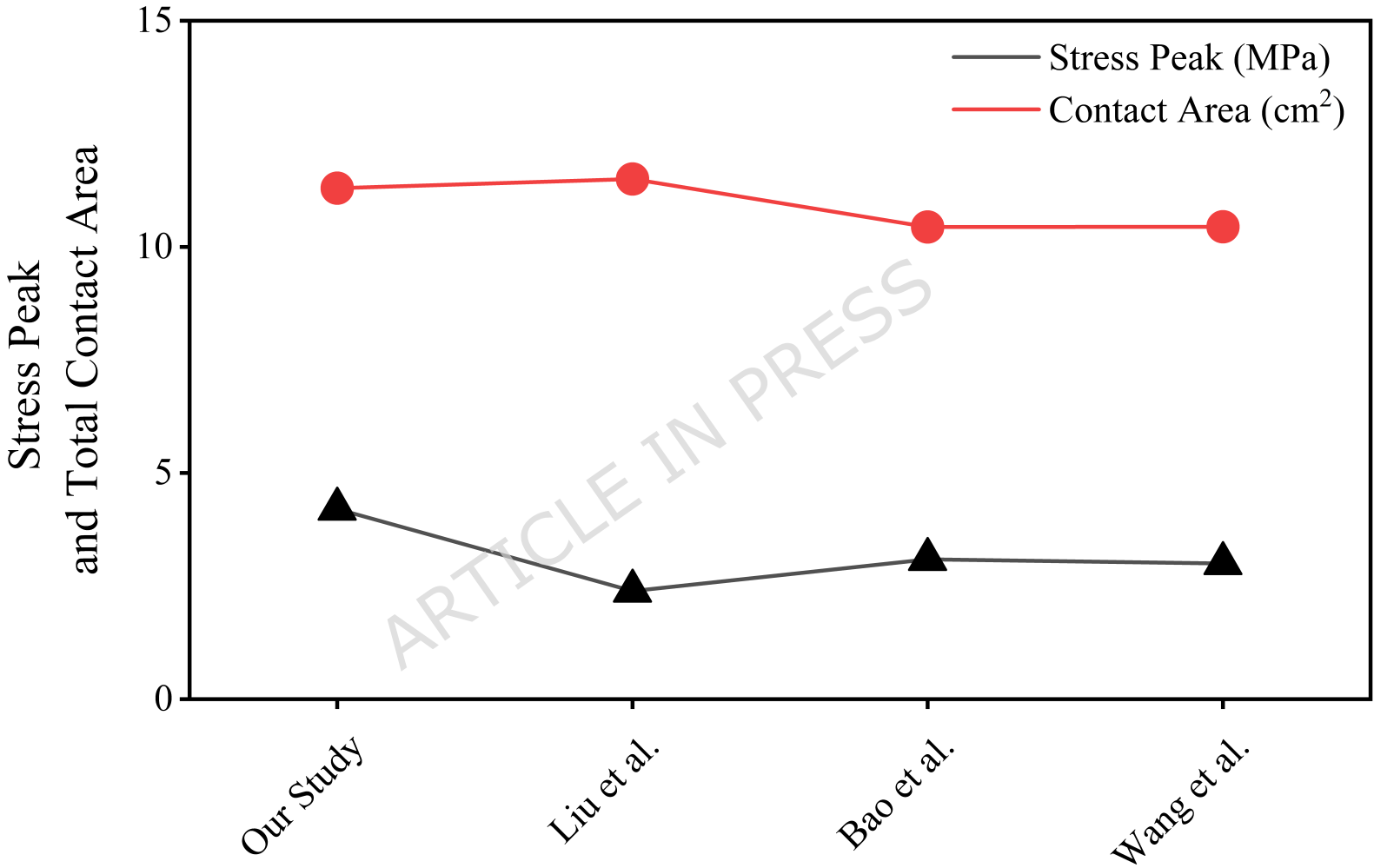

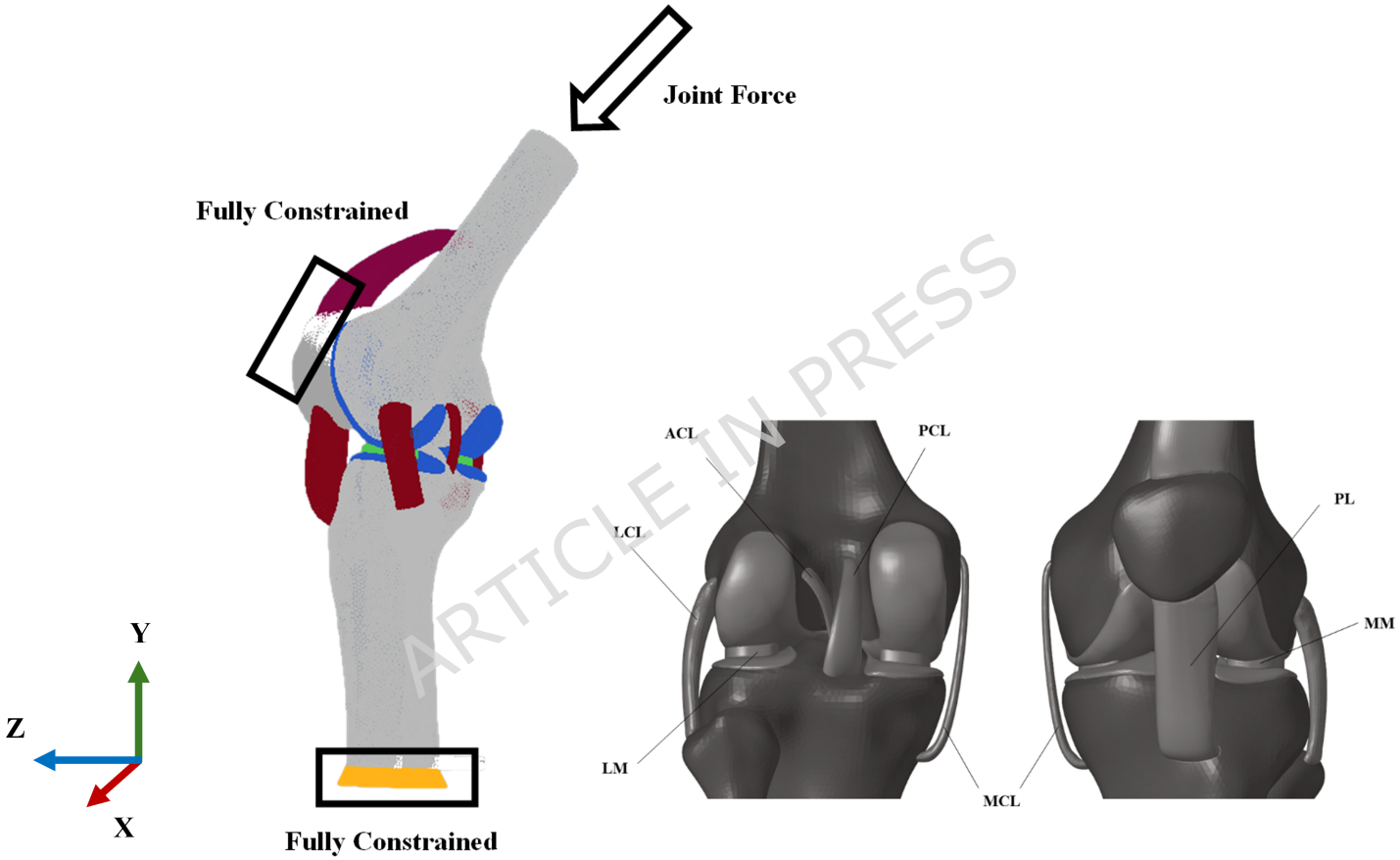

ACL

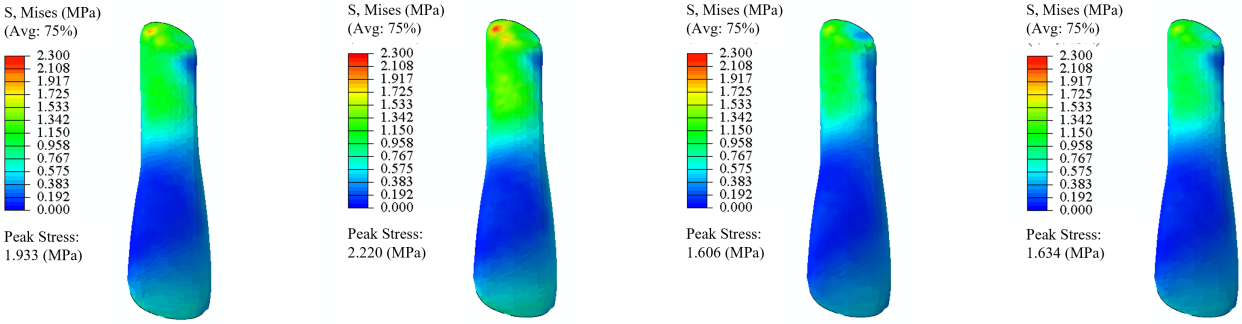

PCL

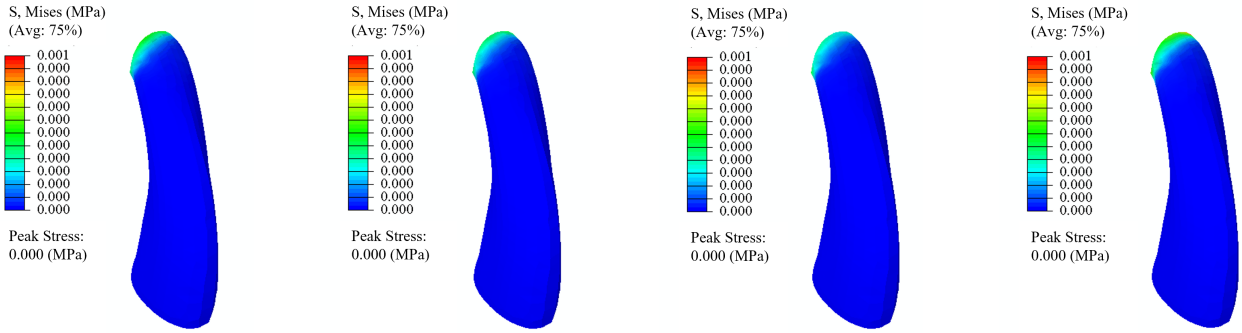

MCL

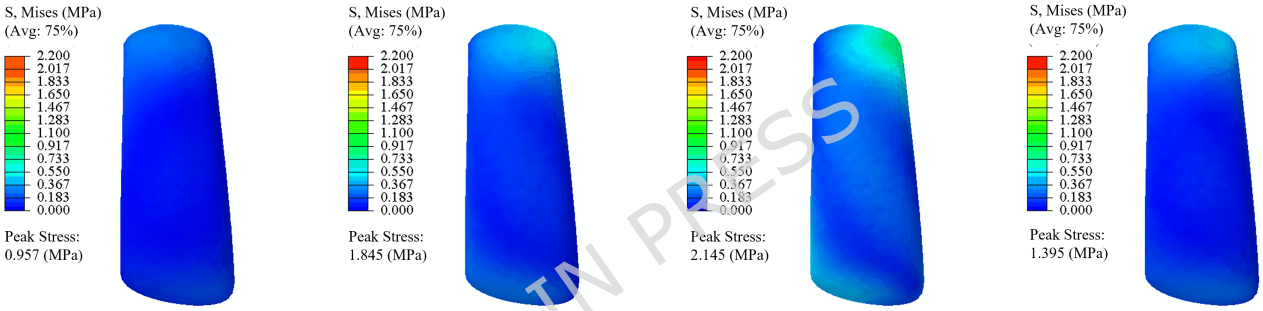

LCL

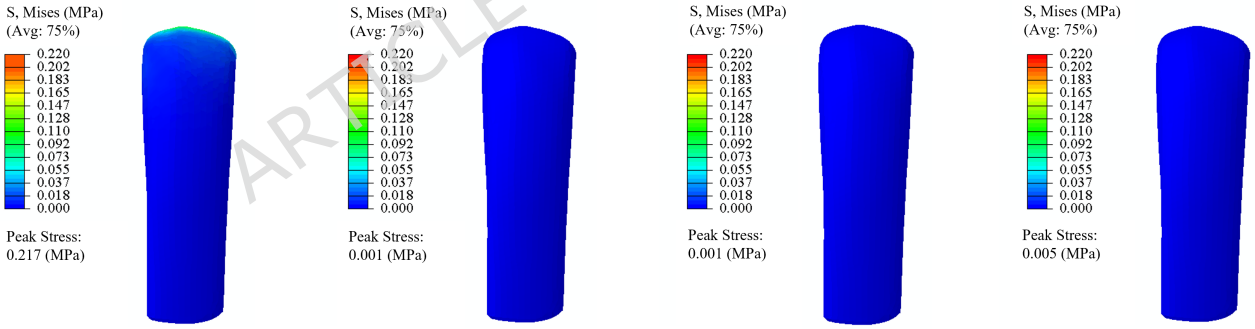

MM

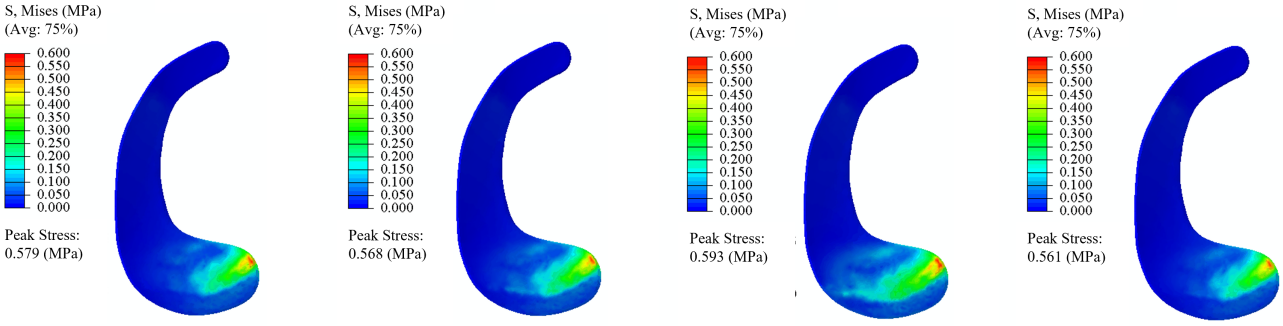

LM

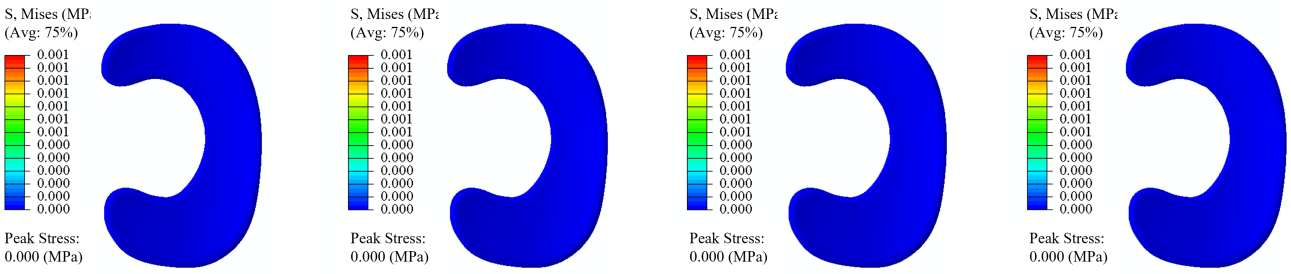

ACL

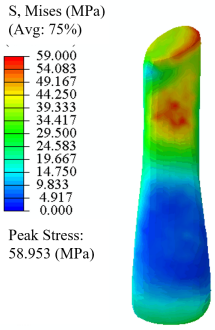

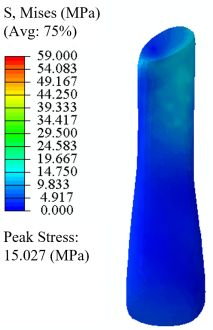

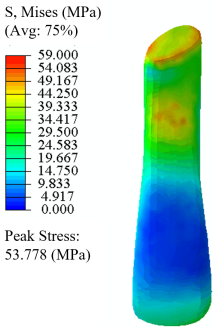

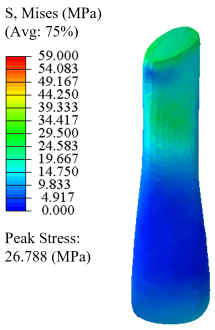

PCL

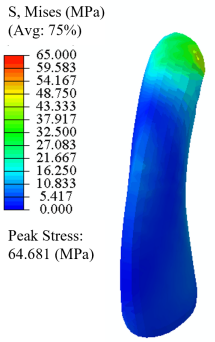

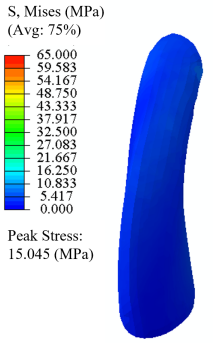

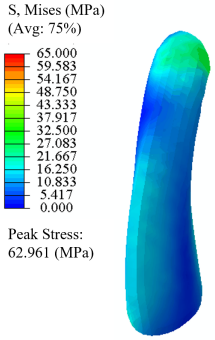

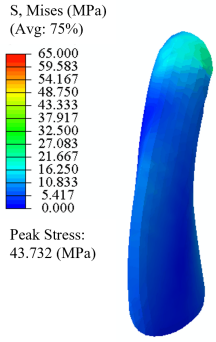

MCL

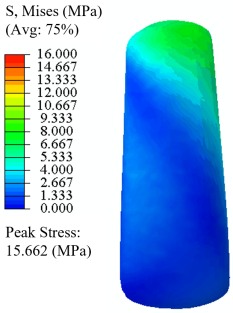

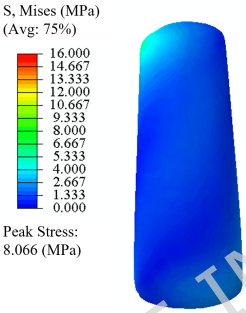

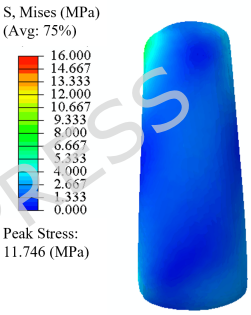

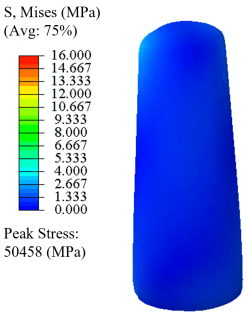

LCL

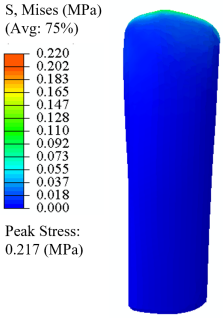

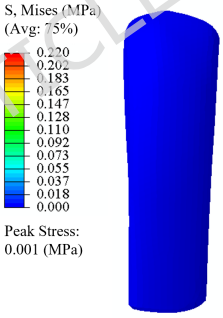

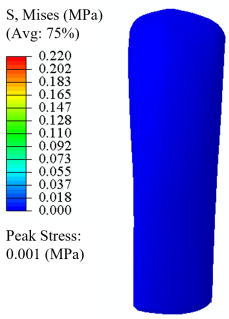

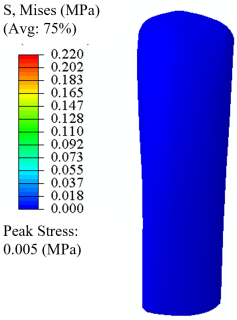

MM

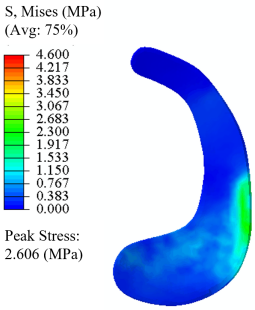

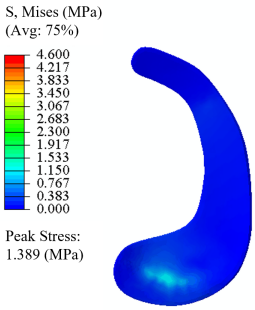

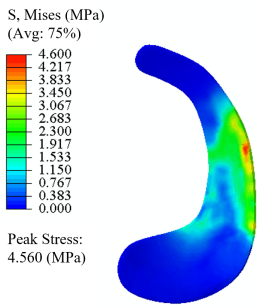

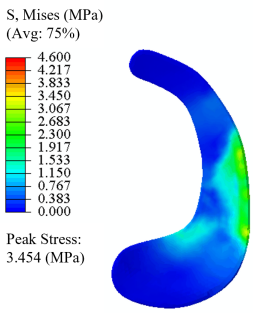

LM

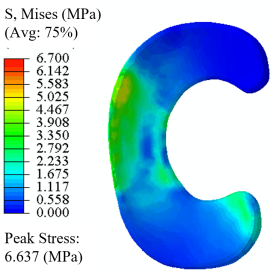

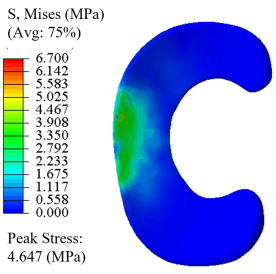

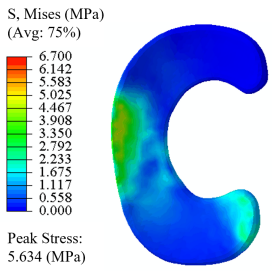

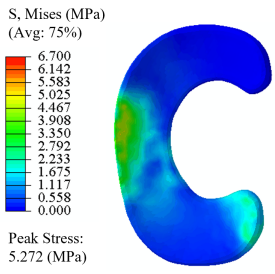

Table 1. Knee Joint Angles and Loads at Preparation Moment to Retraction Moment

Indicator		Preparation Moment			Knee Flexion Moment			Striking Moment			Retraction Moment		
		X	Y	Z	X	Y	Z	X	Y	Z	X	Y	Z
Striking Leg	Joint Angle	-74.45±3.21	-5.06±2.75	5.31±1.88	-122.01±4.02	5.24±2.31	7.72±3.65	-30.72±1.96	2.21±3.44	-5.42±2.02	-39.63±3.53	-28.64±1.85	6.74±2.67
	Joint Force	-1080.88±3.67	285.05±2.91	-344.85±2.14	-940.38±3.52	543.83±3.98	135.28±2.47	52.18±1.76	889.98±4.17	-42.47±3.11	-737.76±2.90	30.10±3.20	397.23±1.97
Supporting Leg	Joint Angle	-45.01±2.14	-18.43±3.33	8.24±1.97	-33.38±3.10	-5.92±2.42	9.39±3.55	-37.44±2.01	-14.95±1.69	8.01±3.04	-32.72±2.78	-13.22±3.31	9.97±2.23
	Joint Force	-986.64±3.24	46.50±2.08	155.70±3.36	-381.69±2.91	-58.94±1.99	749.39±4.12	604.71±3.42	-84.48±2.55	632.12±3.00	729.73±2.10	-306.49±3.77	802.89±2.35

Table 2. Correlation between OpenSim-estimated muscle activations and EMG linear envelopes

Muscle	r	95%CI
Biceps femoris, BF	0.963	0.945 – 0.975
Gluteus maximus, GMAX	0.827	0.752 – 0.881
Lateral gastrocnemius, LG	0.812	0.733 – 0.870
Medial gastrocnemius, MG	0.619	0.480 – 0.728
Semimembranosus, SEM	0.607	0.465 – 0.718
Vastus lateralis, VL	0.586	0.439 – 0.702

Table 3. Material Parameters and Element Properties of the Finite Element Model

Tissue	Elastic Modulus (MPa)	Poisson's Ratio	Element Type
Bone	7300.00	0.30	Hexahedral
Femoral Cartilage	1.00	0.40	Hexahedral
Tibial Cartilage	1.00	0.40	Hexahedral
Meniscus	1.00	0.40	Hexahedral
Medial Collateral Ligament	332.00	0.49	Hexahedral
Lateral Collateral Ligament	345.00	0.49	Hexahedral
Anterior Cruciate Ligament	345.00	0.49	Hexahedral
Posterior Cruciate Ligament	345.00	0.49	Hexahedral
Patellar Ligament	345.00	0.49	Hexahedral